

RESEARCH ARTICLE

10.1029/2018JC014661

Key Points:

- The three-dimensional structure of the offshore export of Mississippi waters is described using observational data and numerical simulations
- The formation and evolution of eddies may affect the low-salinity offshore pathways in the Gulf of Mexico
- This study suggests new insights on the connectivity between remote areas in the Gulf of Mexico

Correspondence to:

Y. Androulidakis,
iandroulidakis@rsmas.miami.edu

Citation:

Androulidakis, Y., Kourafalou, V., Le Hénaff, M., Kang, H. S., Sutton, T., Chen, S., et al. (2019). Offshore spreading of Mississippi waters: Pathways and vertical structure under eddy influence. *Journal of Geophysical Research: Oceans*, 124, 5952–5978. <https://doi.org/10.1029/2018JC014661>

Received 12 OCT 2018

Accepted 30 JUL 2019

Accepted article online 4 AUG 2019

Published online 19 AUG 2019

Offshore Spreading of Mississippi Waters: Pathways and Vertical Structure Under Eddy Influence

Yannis Androulidakis¹ , Vassiliki Kourafalou¹ , Matthieu Le Hénaff^{2,3} , HeeSook Kang¹ , Tracey Sutton⁴, Shuangling Chen⁵ , Chuanmin Hu⁵ , and Nektaria Ntaganou¹

¹Department of Ocean Sciences, Rosenstiel School of Marine and Atmospheric Science (RSMAS), University of Miami, Coral Gables, FL, USA, ²Cooperative Institute for Marine and Atmospheric Studies (CIMAS), University of Miami, Coral Gables, FL, USA, ³NOAA/Atlantic Oceanographic and Meteorological Laboratory (AOML), Miami, FL, USA, ⁴Halmos College of Natural Sciences and Oceanography, Nova Southeastern University, Fort Lauderdale, FL, USA, ⁵College of Marine Science, University of South Florida, St. Petersburg, FL, USA

Abstract The three-dimensional structure of the offshore export of Mississippi River (MR) waters is documented for the first time with in situ data. Numerical simulations and satellite data in the Gulf of Mexico (GoM) are also employed to study two pathways that were detected in summer of 2015, along the eastern and western sides of the Loop Current (LC). The initial formation of offshore branches was primarily due to the interaction of the anticyclonic LC and LC Eddy (which were close to the MR Delta and the Louisiana-Texas shelf-slope, respectively) with riverine waters that had been advected eastward by westerly winds (which reduced the westward buoyancy-driven currents). The interaction of anticyclonic circulation patterns with cyclones (LC Frontal Eddies) was found to influence the dynamics and structure of the branches. Thickness variability and other vertical characteristics of the brackish plumes were investigated from their origin in the northern GoM through their extension in the Straits of Florida. In particular, offshore branch thickness increased near the LC and LC Frontal Eddy fronts. The two types of pathways revealed different factors contributing to the low-salinity waters. Besides the MR input, precipitation contributed to the eastern pathway, while waters from additional northern GoM rivers contributed to the western pathway. The study offers new insights on the processes that control the formation and the offshore (southward) advection of low-salinity waters. These processes have implications on the properties of waters hundreds of kilometers from the northern river sources, extending to the southern Gulf and the Straits of Florida.

1. Introduction

The Mississippi River (MR) discharge is the largest freshwater input into the Gulf of Mexico (GoM) with annual mean rates of over 13,000 m³/s (Morey et al., 2003; Schiller et al., 2011) and flooding conditions that may reach 45,000 m³/s (Androulidakis & Kourafalou, 2013). The neighboring Atchafalaya River contributes about half as much fresh water to the region as the MR. The river plume is thought to mainly affect the circulation processes over the northern GoM (Androulidakis et al., 2015; Schiller et al., 2011; Walker et al., 1994), but there are frequent cases with offshore propagation of brackish water masses toward remote southern GoM areas under the influence of the Loop Current (LC) system (Hu et al., 2005; Morey et al., 2003; Ortner et al., 1995; Schiller & Kourafalou, 2014). Although the flooding discharge rate is a significant precondition for the offshore spreading (Gilbert et al., 1996; Ortner et al., 1995), other conditions such as local (e.g., upwelling-favorable westerly winds, local eddies, and strong stratification in shelf waters) and regional (e.g., LC system) circulation patterns may contribute and enhance the transfer of low-salinity waters away from the Delta (Schiller & Kourafalou, 2014) even during periods without strong outflow rates (Le Hénaff & Kourafalou, 2016).

The offshore spreading of MR waters, which are low in salinity and high in nutrient and sediment content, has been observed in satellite imagery repetitively during summer (Hu et al., 2003, 2005; Nababan et al., 2011). The combination of the seasonal maximum of chl-*a*, occurred usually southeast of the MR in July (Martínez-López & Zavala-Hidalgo, 2009), with the formation of such offshore pathways during summer has also significant biological implications over the broader GoM. Although the near-surface signal of the offshore Mississippi branches has been known, no previous study examined their vertical structure. In

this study, we investigate the formation and three-dimensional evolution of multiple episodes of offshore branches of the low-salinity and highly productive waters under two major pathways, west and east of the main LC system. The use of high-resolution, data-assimilative numerical simulations over the entire GoM, in tandem with data-derived vertical profiles along the offshore pathways, allowed the examination, for the first time, of the vertical structure of these branches that connect the northern Gulf with the central and southeastern GoM regions (e.g., Straits of Florida and their Atlantic exit). The vertical characteristics of these water masses, such as the Brunt Väisälä frequency (indicator for stratification), pycnocline, and Mixed Layer Depth (*MLD*), were examined with respect to the vertical mixing between the deeper clear ocean and the upper brackish layers. Both shelf and basin-wide processes influencing circulation and transport were considered in the analyses.

Several studies have been conducted to explain the circulation of the MR plume west of the Delta over the Louisiana-Texas (LATEX) shelf (i.e., Androulidakis et al., 2015, 2018; Androulidakis & Kourafalou, 2013; Cochran & Kelly, 1986; Dinnel & Wiseman, 1986; Schiller et al., 2011; Zhang et al., 2012) and east of the Delta over the Mississippi-Alabama-Florida (MAFLA) shelf (i.e., Androulidakis & Kourafalou, 2013; Gierach et al., 2013; Schroeder et al., 1987; Walker et al., 1994). The riverine waters originating from the MR Delta are mixed with brackish waters discharged from several other rivers located along the coasts of the LATEX and MAFLA shelves (Figure 1a), following the main circulation patterns of the MR plume. The buoyancy-driven Mississippi plume waters generally reveal two major along-shelf pathways (Kourafalou et al., 1996): a “downstream” coastal current toward the LATEX shelf and an “upstream” current toward the MAFLA shelf (Androulidakis et al., 2015; Schiller et al., 2011; Zhang et al., 2012). Walker et al. (1994) and Gilbert et al. (1996) described the properties of the low-salinity waters that originated from the Mississippi and reached the Atlantic Ocean during the 1993 flood, entrained in the shoreward edge of the LC and the Florida Current (FC) throughout the Straits of Florida. They showed that brackish waters with salinity as low as 31 were detected 40-km offshore of the Florida Keys for about 3 months, affecting the upper 30 m of the water column. The same event was also discussed by Ortner et al. (1995), who showed that the eastward components of the winds around the MR Delta, opposed to the downstream transport, also contributed to the accumulation of brackish waters south of the Delta, where the extended LC was present. Yuan et al. (2004) studied such offshore export under the effect of tropical storms that may carry nutrient-rich MR waters to the open Gulf. The intrusion of MR waters in the Gulf Stream of Georgia was described by Atkinson and Wallace (1975) and Hu et al. (2005), reaching all the way to Cape Hatteras (Atkinson & Tester, 1993). The MR impacts on the regional climate of the GoM and on the transport over the broader Atlantic Ocean were also discussed by Nürnberg et al. (2008).

The main goal of the current study is to examine the full three-dimensional structure along the offshore Mississippi branches and to investigate the effects of the regional circulation features such as the LC system and the accompanying cyclonic LC Frontal Eddies (LCFEs), on their dynamical and structural characteristics during the summer of 2015. This period is a particularly good case study for investigating the offshore MR pathways, as it started with significant quantities of freshwaters discharged in the northern GoM (Table 1; Fournier et al., 2016). The surface signal of the offshore MR water export in the summer of 2015 was also described by Chen and Hu (2017) to evaluate their method for estimating Sea Surface Salinity (SSS) from satellite ocean color measurements. They showed, based on both in situ (R/V Walton Smith; University of Miami) and satellite surface observations, that northern Gulf brackish waters reached the Florida Keys. In this study, we use a combination of unique tools that allow us to study three successive episodes of offshore export of brackish waters that occurred in July and August of 2015: two episodes along the eastern LC boundary (eastern pathway) and one episode along the western LC boundary (western pathway). Furthermore, we advance all previous studies of MR offshore water removal by asking the following novel questions: (1) What is the origin of the brackish waters along each MR offshore branch? (2) Is the MR Delta the major source of low-salinity waters exported to the GoM interior, in relation to other freshwater sources such as rainfall and inputs from the other northern GoM rivers? (3) What is the three-dimensional structure of these offshore MR branches that can reach remote Gulf coastal areas? (4) Were the favorable conditions (rivers, meteorological, and oceanographic) similar during the three episodes? To answer these questions, we use high-resolution, data-assimilative modeling; satellite remote sensing; and glider measurements, as well as in situ data from the Deep Pelagic Nekton Dynamics of the Gulf of Mexico (DEEPEND; <http://www.deependconsortium.org/>) Consortium of the Gulf of Mexico Research Initiative.

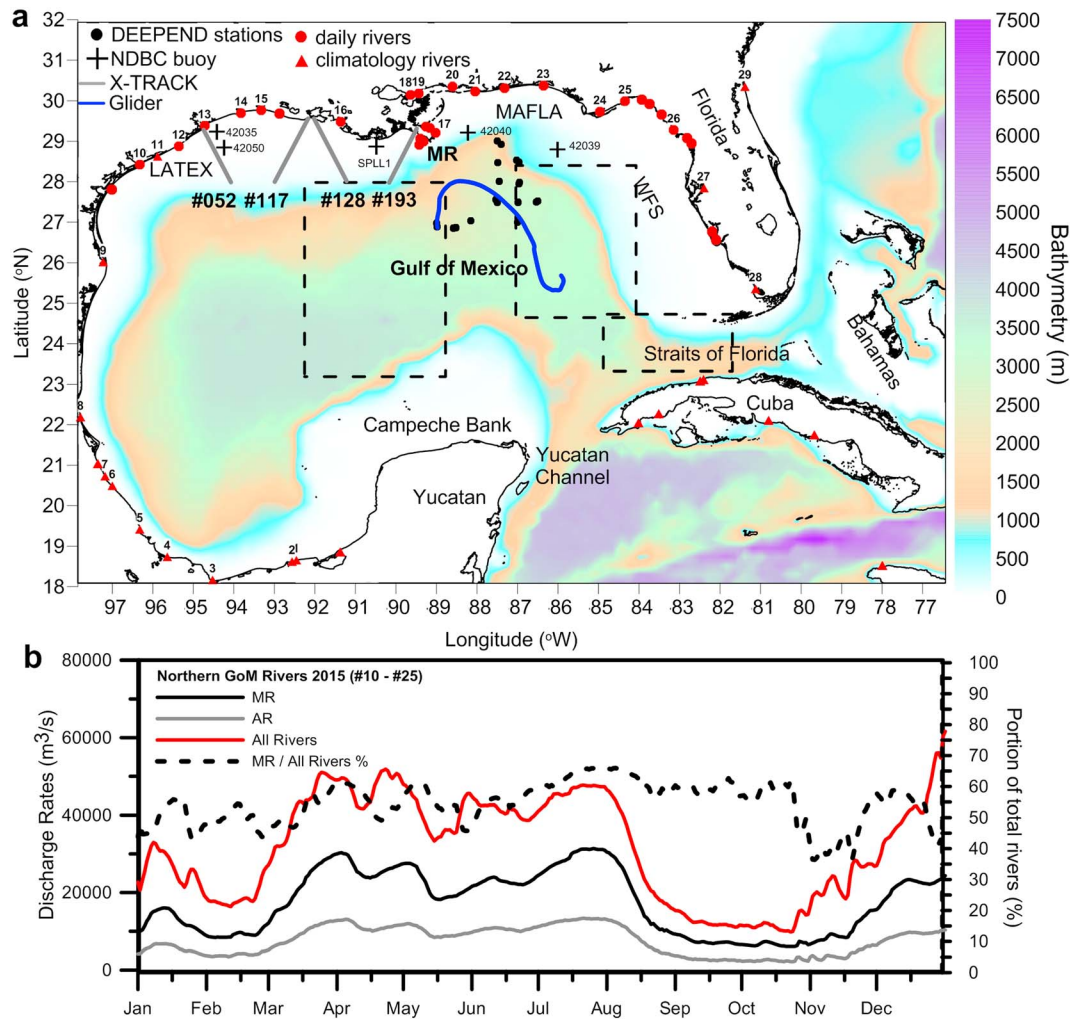


Figure 1. (a) Bathymetry of Gulf of Mexico Hybrid Coordinate Ocean Model (GoM-HYCOM 1/50) domain (depth color scale in meters) indicating the main topographic features (Cuba, Straits of Florida, Campeche Bank, Florida, WFS, LATEX, MAFLA, Yucatan Channel, Bahamas, and MR). The locations of DEEPEND stations (black dots), Glider track (blue line), and NDBC buoys (crosses) are marked. The Jason-2 Tracks 52, 117, 128, and 193 from the coast to 28°N are indicated with gray lines. Rivers with annual mean discharge greater than 50 m³/s are assigned numbers; smaller rivers are only marked. Rivers with daily discharge values are in red circles, and rivers with monthly climatology discharge values (mainly in Mexico and Cuba) are in red triangles. Dashed boxes indicate the areas used in Figure 14 (western and eastern branches and Straits of Florida). (b) Daily evolution, in 2015, of the MR (black line) and of AR (gray line) and total discharge daily rates (m³/s) of all northern Gulf of Mexico rivers (red line), marked with numbers 10–25 in (a). The dashed line indicates the ratio (%) between MR and total river discharges. LATEX = Louisiana-Texas; MR = Mississippi River; WFS = West Florida Shelf; MAFLA = Mississippi-Alabama-Florida Shelf; NDBC = National Data Buoy Center; AR = Atchafalaya River.

The methods and data used in this study are described in section 2. The outflow characteristics of all GoM rivers, presented in Figure 1 and Table 1, are also described in section 2. Section 3 presents a vertical and horizontal validation of the simulations against the DEEPEND data set of observations and a detailed description of the main riverine pathways formed in the summer of 2015. The regional circulation effects on the evolution of the offshore branches, the respective upper-ocean vertical characteristics, and the origin of the brackish waters are discussed in section 4. Finally, a summary of concluding remarks is presented in section 5.

2. Data and Methods

2.1. Observations

2.1.1. In Situ Measurements

Measurements of physical properties (temperature and salinity; Conductivity-Temperature-Depth: CTD) from a DEEPEND cruise (DP02), conducted over the central-northern GoM during the period of 09–21

Table 1
Monthly and Annual Mean River Discharges ($10^2 \text{ m}^3/\text{s}$) along the Gulf of Mexico Coastline for 2015

No	River name	J	F	M	A	M	J	J	A	S	O	N	D	Mean
1 ^a	Grijalva	1.3	1.4	1.3	1.5	1.5	1.5	1.2	1.2	1.2	1.6	1.8	1.7	1.4
2 ^a	Rompido de Samaria	3.5	3.6	2.3	2.4	2.7	4.7	8.5	10.0	13.2	10.7	5.6	3.9	5.9
3 ^a	Cortzacoalcos	2.3	1.8	1.2	0.8	0.7	2.6	6.0	9.4	11.3	6.1	3.8	3.6	4.1
4 ^a	Papaloapan	6.1	5.7	5.3	5.5	5.4	10.6	14.5	14.9	17.4	11.7	8.0	6.5	9.3
5 ^a	La Antigua	0.3	0.3	0.2	0.2	0.0	0.4	0.8	0.9	1.2	1.0	0.5	0.4	0.5
6 ^a	Tercolutla	1.0	0.8	0.7	0.6	0.9	2.3	2.8	3.4	4.5	3.8	1.9	1.1	2.0
7 ^a	Bobos	0.5	0.4	0.3	0.2	0.3	0.6	0.6	0.6	1.1	1.0	0.7	0.5	0.6
8 ^a	Paunuca	1.7	1.4	1.3	1.2	1.5	4.4	8.3	7.5	13.8	10.2	3.8	2.4	4.8
9 ^a	Rio Grande	1.5	1.5	1.6	1.5	1.3	0.9	0.5	0.5	0.5	0.6	0.7	1.1	1.0
10	Guadalupe, Lavaca	0.2	0.2	1.3	1.3	2.9	3.7	0.7	0.3	0.3	0.5	1.5	0.7	1.1
11 ^a	Colorado	1.1	1.1	1.1	1.1	0.9	0.7	0.4	0.3	0.4	0.4	0.5	0.8	0.7
12	San Bernard, Brazos	2.2	0.9	5.0	3.3	10.1	15.9	6.3	1.6	0.8	2.1	8.9	10.3	5.6
13	San Jacinto Conore-Porter, Brays Bayou	4.0	0.7	7.5	3.9	16.1	16.4	6.6	2.3	1.0	1.5	12.1	13.8	7.2
14	Village, Neches, Sabine	6.8	3.1	9.7	10.3	12.3	12.1	6.4	2.9	2.3	1.7	7.3	7.1	6.8
15	Calcasieu	1.1	0.2	1.2	1.5	1.1	0.6	0.2	0.1	0.1	0.1	2.0	0.6	0.7
16	Atchafalaya	55.1	39.8	93.3	114.2	97.6	104.8	126.8	81.5	28.2	25.0	41.4	90.3	74.8
17	Mississippi	96.3	68.7	163.4	198.7	163.3	171.0	217.7	137.7	55.9	49.5	76.2	161.1	129.9
18	Amite, Tangipahoa	1.3	0.5	1.9	1.1	1.1	0.8	0.6	0.3	0.2	1.6	2.4	1.0	1.1
19	Pear, Bogue Chitto	4.5	2.1	7.2	4.2	2.1	2.2	1.1	0.7	0.6	0.9	3.7	3.1	2.7
20	Pascagoula, Red Creec	5.2	2.0	6.0	3.9	1.7	1.3	1.1	0.5	0.4	0.6	3.3	4.4	2.5
21	Tombigbee, Alabama	18.0	16.4	27.6	30.8	10.6	7.1	6.1	4.1	2.8	3.4	14.6	24.9	13.9
22	Escabia Century-Molino, Blackwater, Yellow Miligan, Shoal	4.2	2.8	3.5	5.8	2.8	2.2	1.5	1.0	1.0	1.4	4.8	8.5	3.3
23	Choctawhatchee	3.5	2.7	3.2	5.4	2.9	2.4	1.7	1.2	1.1	2.3	6.9	6.9	3.3
24	Chipola, Apalachicola	15.9	12.8	15.4	16.6	11.6	9.2	6.5	5.7	5.6	6.8	15.9	24.5	12.2
25	Ochlockonee	3.0	1.9	1.7	1.1	0.5	0.3	0.4	0.4	0.2	0.1	0.6	0.5	0.9
26 ^a	Suwannee	7.6	7.7	7.5	4.3	3.1	1.6	1.7	2.2	2.9	2.1	1.7	1.8	3.7
27 ^a	Hillsborough	1.8	1.8	2.0	0.4	0.4	0.4	0.2	0.3	0.9	0.5	0.0	0.3	0.8
28 ^a	Shark River	3.6	0.8	2.2	0.6	0.9	9.0	15.3	16.2	17.7	12.8	9.4	8.4	8.1
29	Saint Johns	1.3	1.3	1.4	1.4	1.2	0.9	0.5	0.4	0.5	0.6	0.6	1.0	0.9

Note. Rivers are numbered clockwise, starting from Mexico, through the U.S. coast and over northern Cuba (following Figure 1a). Mean values are computed from either daily measurements or from monthly climatology. Only rivers with annual mean discharge rates over $0.5 \times 10^2 \text{ m}^3/\text{s}$ are listed.

^aRivers with climatology discharges.

August 2015 on the R/V *Point Sur* (Figure 1a), were used to evaluate the numerical simulations and to describe the vertical structure of the water column inside and outside the MR offshore branches. The vertical profiles covered the upper 1,500 m of the water column with approximately 1-m vertical step.

Wind measurements, collected every hour at four National Data Buoy Center (NDBC) buoys (Figure 1a), were used to describe the wind conditions around the MR Delta (Buoy SPL11 from Louisiana State University and Buoy 42040), over the LATEX (Buoy 42035) and MAFLA (Buoy 42039) shelves in addition to half-hour near-surface (2 m) current data on the LATEX shelf (Buoy 42050, from Texas A&M University). In addition, 3-hourly precipitation data on the 0.125° grids were derived from the European Centre for Medium-Range Weather Forecasts (ECMWF; <https://www.ecmwf.int>) to identify the relative contribution of precipitation and river runoff on low-salinity waters along the offshore branches in the central GoM and in remote areas, such as the Straits of Florida.

A Slocum glider was also deployed from the R/V *Point Sur* within the DEEPEND study area (approximately at 89°W , 27°N ; Figure 1a) during the DEEPEND DP02 cruise on 9 August 2015 (USF). The glider operated from 2- to 200-m depth until 10 August, after which the dive profiles were changed to 400 m. For the present study, we used the vertical profiles of the upper 100 m to investigate the vertical structure of the upper-ocean along the LC periphery. The glider was initially scheduled to cross the LC and exit to the west but it ended up being entrained by the LC, thus providing unique information about the physical properties and speed of the LC. It was recovered on 22 August, near 86°W , 25.5°N .

2.1.2. Satellite Observations

Three types of satellite data were used in this study. The first one includes ocean color maps, derived from the Moderate Resolution Imaging Spectroradiometer (MODIS) Aqua satellite. These maps are part of a GoM Coastal Ocean Observing System product, developed and distributed by the Optical Oceanography Laboratory from USF (<http://optics.marine.usf.edu/>). These data comprised 7-day composites of chl-*a* concentration (mg/m^3) at the ocean surface layer with 1-km spatial horizontal resolution. In this study, the 1-km resolution data were aggregated to 4-km resolution in order to better observe offshore eddies and other features. The high chl-*a* concentrations at the surface provide information about the river plume pathways both over the northern shelves (LATEX and MAFLA) and the far-field regions (central GoM and the Straits of Florida). In contrast, the clearer LC waters are usually characterized by low chl-*a* concentrations (Hu et al., 2005). A second satellite product used in this study and also derived from the MODIS observations is SSS weekly estimates at 1-km resolution (Chen & Hu, 2017). This novel MODIS SSS product provides much higher resolution than the direct SSS measurements of the Aquarius satellite (~ 150 km). It was developed from a machine-learning approach using extensive field and satellite data and was validated thoroughly for offshore plumes (Chen & Hu, 2017). The product was applied to validate the model simulations and to confirm the extensions of low-salinity waters over the entire GoM during the summer of 2015 in tandem with the available in situ observations and satellite chl-*a* maps.

Finally, altimetry data from Jason-2 were extracted along four satellite tracks available at the Center of Topography of the Oceans and the Hydrosphere (CTOH, <http://ctoh.legos.obs-mip.fr/>). A high-resolution (less than 0.05°) along-track data set was thus derived along Tracks 117, 193, 052, and 128 (Figure 1a), which covered the MR Delta, and the northwestern continental shelf from the deep areas to the coast. CTOH computes and distributes specific, coastal, along-track Sea Level Anomalies using the X-TRACK software (Cancet et al., 2009; Roblou et al., 2011). The altimeter data were selected for June 2015 and August 2015, two periods with different evolutions of the downstream current along the LATEX shelf, crucial for the formation of offshore pathways (see section 3.2). Similar X-TRACK products were used by Kourafalou and Androulidakis (2013) to describe the evolution of the westward downstream current over LATEX during the Deepwater Horizon oil spill period in 2010. The most apparent buoyant patterns, and especially the westward geostrophic coastal current (Garvine, 1987; Hickey et al., 1998; Kourafalou et al., 1996; Kourafalou & Androulidakis, 2013), can be estimated by the total sea surface slopes in successive points of the satellite tracks.

2.1.3. River Outflow Characteristics in 2015

The major rivers of the GoM are marked in Figure 1a. The respective monthly mean outflow rates for 2015 with annual means larger than $50 \text{ m}^3/\text{s}$ are presented in Table 1. The discharge values were derived from either daily measurements obtained through the U.S. Geological Survey (<https://www.usgs.gov/>) and the Army Corps of Engineers or monthly climatology. The majority of the rivers is located over the northern Gulf along both LATEX and MAFLA coastlines. The MR monthly mean outflow rates were significantly higher in July 2015 ($>21,000 \text{ m}^3/\text{s}$; Table 1) with daily values higher than $30,000 \text{ m}^3/\text{s}$ in late July, more than double the July climatological mean ($\sim 13,000 \text{ m}^3/\text{s}$; Androulidakis & Kourafalou, 2013). The daily outflow rates were used as freshwater input in the numerical simulations (see section 2.2). They were also used to investigate the river effects on the formation of the river plumes and to the evolution of the offshore low-salinity pathways.

The combined discharge of all northern rivers revealed successive high peaks from March to August, exceeding $50,000 \text{ m}^3/\text{s}$ (Figure 1b). The largest discharge rate among the LATEX rivers (#10 to #16 in Table 1 and Figure 1a) was observed for the Atchafalaya River, revealing a significant peak in July 2015, the same month as for the MR. The second highest LATEX outflow was observed 1 month earlier for San Jacinto, Conore-Porter, and Brays Bayou rivers, located around 95°W (Table 1 and Figure 1a). Although more rivers are located along the MAFLA shelf (#18–28) in comparison to the LATEX shelf (Figure 1a), the total annual mean discharge of LATEX rivers is almost double ($969 \text{ m}^3/\text{s}$) the respective rate of the MAFLA rivers ($525 \text{ m}^3/\text{s}$), mainly due to the large discharge from the Atchafalaya river (Table 1). All rivers contribute to the freshwater input to GoM, but the major suppliers are the MR, followed by the Atchafalaya River (Table 1), where about a third of the Mississippi catchment area is drained through man-made diversions (Meade & Moody, 2010). During the August peak, the MR supplied 70% of the riverine freshwater into the Gulf, while the total values of the rest of the rivers exceeded the MR contribution mainly in November

(Figure 1b). In addition, the MR contribution was reduced in late May and early June, when the ratio of MR/Total Rivers was around 50%, indicating the large freshwater input from other rivers in that period (Figure 1b).

2.2. GoM-HYCOM Model Simulations

The 2015 simulation is based on the implementation of the Hybrid Coordinate Ocean Model (HYCOM) in the GoM with high resolution ($1/50^\circ$, ~ 1.8 km) and 32 hybrid vertical layers (GoM-HYCOM 1/50; Le Hénaff & Kourafalou, 2016). The hybrid mode of the model optimizes the distribution of vertical layers by making them isopycnal in stratified water columns, terrain-following sigma in coastal regions, and isobaric in the mixed layer and very shallow areas (Bleck, 2002; <https://hycom.org/>). This unique utility in combination with the special treatment of freshwater inputs (Schiller & Kourafalou, 2010) also makes HYCOM advantageous in areas with complicated topography (Figure 1a) and strong freshwater outflows such as the MR discharge (Androulidakis & Kourafalou, 2013; Kourafalou & Androulidakis, 2013; Le Hénaff & Kourafalou, 2016; Schiller et al., 2011) and allows the development of detailed process studies around the outflow regions, where plume dynamics are dominant (Androulidakis et al., 2015).

The GoM-HYCOM 1/50 domain covers the entire Gulf and the adjacent areas in the Caribbean Sea and the Straits of Florida, connecting the Gulf with the Atlantic Ocean (Figure 1a). The 2015 model archives employed here are part of a long-term simulation system that also provides 7-day forecasts of the GoM on a weekly basis, operated by the Coastal and Shelf Modeling Group at the Rosenstiel School of Marine and Atmospheric Science, University of Miami (<http://coastalmodeling.rsmas.miami.edu/>). Daily river discharges were implemented at 34 major river mouth locations, after merging and dividing of 54 river discharge estimates, while monthly climatological river discharges were represented at minor river mouth locations (Figure 1 and Table 1). MR daily discharge is implemented at six passes, effectively representing the MR passes through the Delta. The open boundary conditions are provided by the operational GLoBal HYCOM simulation run by the Naval Research Laboratory (<https://www.nrl.navy.mil/>). For 2015, we used the GLoBal HYCOM expt_91.1, available at hycom.org. The GoM-HYCOM 1/50 was forced by the 3-hourly winds, thermal forcing, and precipitation on the spatial resolution of 0.125° produced by ECMWF and distributed through the Meteorological Archival and Retrieval System.

The GoM-HYCOM 1/50 uses data assimilation in order to simulate realistic ocean features. The data assimilation scheme used in this study is based on the sequential static ensemble optimal interpolation filter as described by Le Hénaff and Kourafalou (2016), based on Halliwell et al. (2014, 2015). The model error covariance matrix is estimated from a long, free-running simulation of the same model with the same configuration (Le Hénaff & Kourafalou, 2016). The 2015 simulation assimilates along-track altimetry data (from Jason-2, SARAL-AliKa, CryoSat-2, and HY-2A) distributed by Archiving, Validation and Interpretation of Satellite Oceanographic (AVISO), Sea Surface Temperature (SST) from U.S. Navy's Multichannel SST data set that is available on the U.S. Global Ocean Data Assimilation Experiment server (<http://usgodae.org>), and in situ observations: SST from buoys, ship cruises, and surface drifters, as well salinity and temperature profiles from Argo floats and Expendable Bathythermograph (XBT) casts. In the 2015 run, the assimilation of altimetry data has been upgraded with respect to the implementations of the same filter in Le Hénaff and Kourafalou (2016). In that previous implementation, the quantity that was assimilated was the anomaly of the observed along-track Absolute Dynamic Topography (ADT) with respect to the spatial mean of the ADT over the GoM on the same day, a similar treatment being applied to the model Sea Surface Height (SSH) for consistency. In the present study, we consider the anomalies of the simulated SSH with respect to a mean SSH estimated from a 3-year reference simulation (2010–2012) that uses the previous implementation of the data assimilation filter that was just described, and we then assimilate the anomaly of the observed along-track ADT with respect to the mean observed ADT during the same 3-year period. This modification allows the data assimilation filter to constrain not only the mesoscale features that are observed along individual satellite tracks but also the low-frequency changes, such as the steric signal.

Two additional simulations without MR input (*NoMR* experiment) and without both MR and precipitation input (*NoMR/NoPrecip* experiment) but with the same realistic initial, boundary, and atmospheric conditions (other than the precipitation for the second case) were also performed for 2015, in order to elucidate

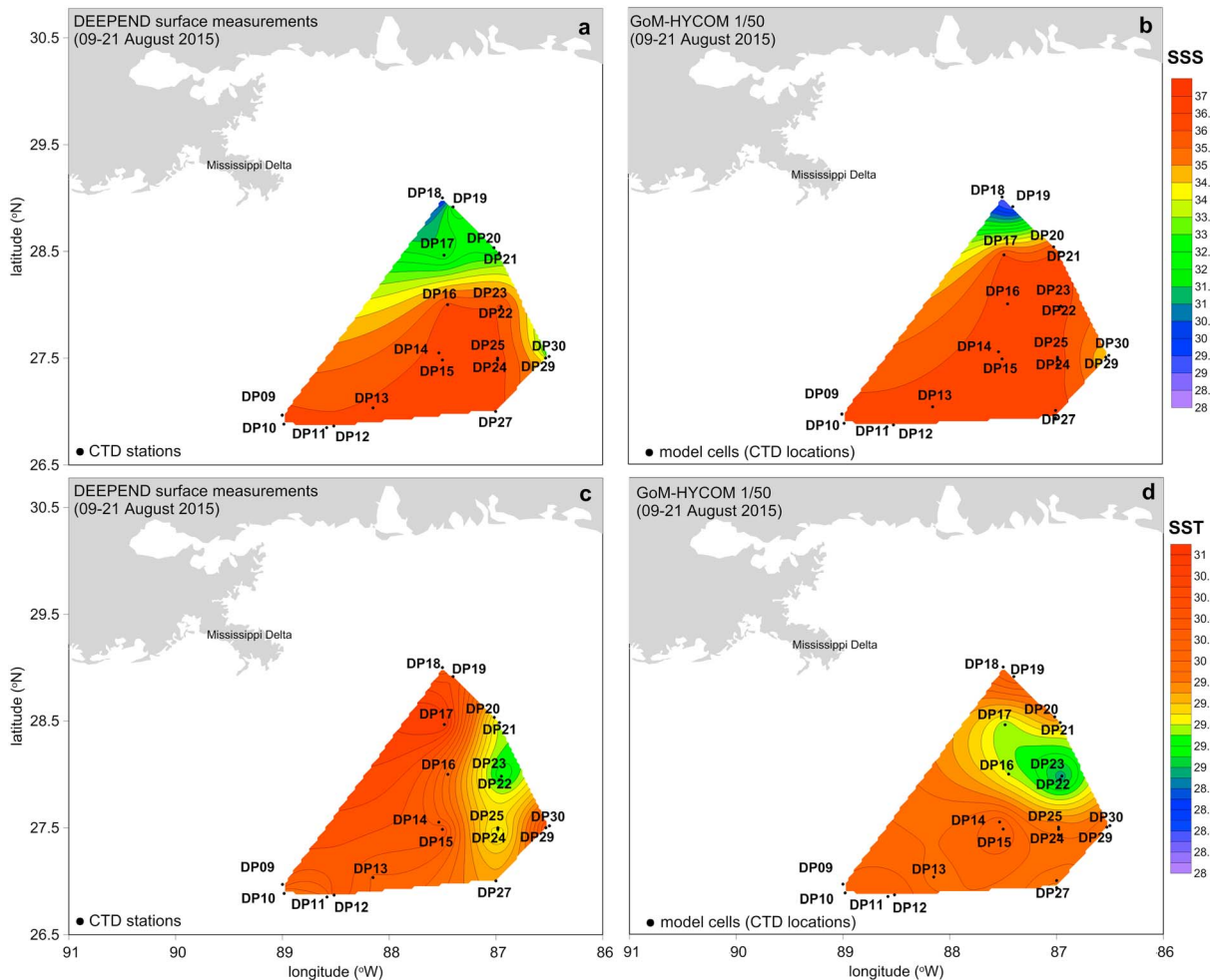


Figure 2. Comparison of measured (DEEPEND) and simulated (GoM-HYCOM 1/50) values at the same locations and for the period 9 to 21 August 2015. (top panels) Distribution of (a) in situ and (b) simulated SSS (contour lines every 1 unit). (bottom panels) Distribution of (c) in situ and (d) simulated SST (contour lines every 0.1 °C). GoM-HYCOM = Gulf of Mexico Hybrid Coordinate Ocean Model; SSS = Sea Surface Salinity; SST = Sea Surface Temperature.

the different factors influencing salinity during the formation and evolution of the offshore brackish pathways (see section 4.3).

3. Results

The representation of circulation related to river plume dynamics by GoM-HYCOM 1/50 has already been evaluated against observations by Le Hénaff and Kourafalou (2016), who described the offshore pathways of MR waters under no flooding conditions in 2014. In section 3.1, we present additional model evaluation, comparing the simulated results against in situ DEEPEND vertical profiles available along the eastern pathway during the summer of 2015. This evaluation shows that the model can adequately simulate both surface and upper-ocean physical processes. We also used satellite data (ocean color, salinity, and coastal altimetry) in tandem with respective model fields, for additional model evaluation and to identify the major pathways of the brackish waters during summer of 2015 (section 3.2). None of these data sets was assimilated in the numerical simulations, which ensures that the evaluation was performed with independent data.

3.1. Model Evaluation

The surface distribution of salinity, measured during the DEEPEND cruise during the period of 09–21 August 2015, is presented in Figure 2a. Low-salinity waters (~31) were detected over the northern stations in agreement with the simulated salinity (Figure 2b). These low-salinity values are associated with an offshore brackish branch, located north of 28.5°N. We will discuss about that pathway in more detail in

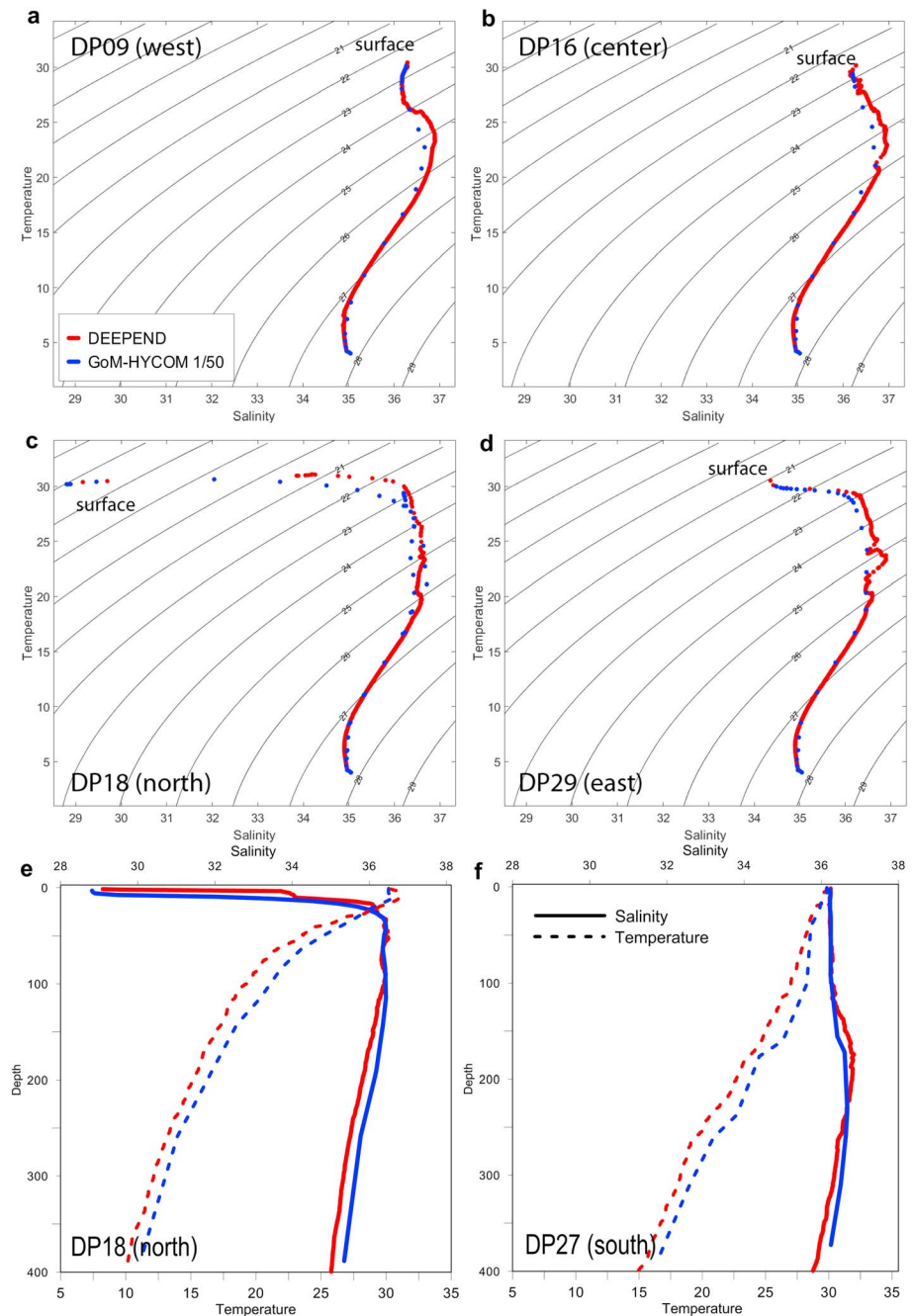


Figure 3. T/S diagrams derived from simulated (blue) and measured (red) temperature and salinity pairs at (a) DP09, (b) DP16, (c) DP18, and (d) DP29 stations. The values represent the entire water column (down to the deepest DEEPEND measurement). Surface values are marked, and the geographical placement of each station is given in parentheses, for orientation (stations marked in Figure 2). Black lines in T/S diagrams represent the isopycnal contours with 1 kg/m³ step. The vertical profiles of simulated and measured salinity (solid) and temperature (dashed) over the upper 400 m are also presented for (e) DP18 and (f) DP27 stations. GoM-HYCOM = Gulf of Mexico Hybrid Coordinate Ocean Model.

section 3.2. The highest salinity values were detected over the central and southern areas in both measured and simulated surface salinity. In both cases, the salinity contours revealed higher values (>36) in the central area (87.5°W) and relatively lower values (~35) over the western (~88°W) and eastern (~87°W) part of the observational grid. Similarly, the surface temperature spatial distribution shows good agreement between the DEEPEND observations (Figure 2c) and the GoM-HYCOM 1/50 simulations (Figure 2d), with cooler waters over the eastern area in both fields, probably associated with a LCFE. The upwelling within

cyclonic eddies may have led to lower temperature of the surface waters. We note that the model can produce surface circulation patterns characterized by both salinity and temperature gradients.

The Temperature/Salinity (T/S) diagrams in Figure 3 present the vertical profiles of salinity, temperature, and density at four characteristic stations in the western (DP09), central (DP16), northern (DP18), and eastern (DP29) parts of the DEEPEND data grid. The surface density values are around $1,023 \text{ kg/m}^3$ at both western and central areas, while at the deepest layers, the density are close to $1,028 \text{ kg/m}^3$. The physical characteristics of the deepest layers were almost the same at all stations, showing temperature values below 5°C and salinity around 35. The presence of riverine waters was captured at the eastern station DP29 (Figure 3d) and especially at the northern tip of the grid (DP18), where density ranges between 1,017 and $1,021 \text{ kg/m}^3$ (Figure 3c). The simulated and observed vertical profiles of the northernmost DEEPEND station show that the river plume covered the upper 40 m of the water column at this region (Figure 3e) with salinity values ranging from 29 (surface) to 36 ($\sim 35 \text{ m}$). In contrast, salinity was higher than 36 from the surface to 400 m at the southernmost stations DP27 (Figure 3f). An underwater salinity maximum, which is the signature of the Subtropical Underwater that is entrained from the Caribbean Sea to the GoM by the LC (Merrell & Morrison, 1981), was detected between 150 and 200 m in both measured and simulated profiles. Significant differences were also observed in the temperature profiles of DP18 and DP27. Although both areas revealed surface values around 30°C , the vertical distribution was different below 30 m with a strong thermocline between 50 and 100 m for the DP18 station and a smoother decrease along the entire water column at the DP27 station. The upper 35-m layer at the DP18 station was affected by the brackish waters showing homogenous temperature distribution from the surface to the base of the river plume. Both simulations and measurements showed that the 400-m layer was significantly colder over the northern (10°C) than the southern (15°C) area, which was located inside the warm LC body on August 2015 (see section 3.2). The overall agreement between the model results and the measured parameters is remarkable, supporting the ability of the model to describe the vertical structure, although no DEEPEND data were assimilated in the simulations. Such a good comparison in 3-D salinity structure, especially at data points near strong gradients, is generally very challenging to achieve in ocean modeling.

The overall temperature comparisons (vertical and horizontal) between DEEPEND measurements and GoM-HYCOM 1/50 simulations are presented in Figure 4a. Their linear fit shows that the majority of the compared pairs are located along the 1:1 identity line, revealing very high Pearson correlation coefficient ($r_{\text{pearson}} = 0.99$) and coefficient of determination ($R^2 = 0.98$). The difference between the simulated and observed means is around 0.5°C , while the agreement is very good, especially for cold ($<10^\circ\text{C}$) and warm ($>28^\circ\text{C}$) water masses. The salinity comparison highlights the ability of the model to represent the ocean salinity in both river plume and clear ocean areas (Figure 4b). Although the agreement is lower in values below 34, the Pearson correlation is around 0.60, and the majority of the pairs are also located along the $x = y$ line, especially between 34 to 37 values, despite a few outliers. The difference between the mean values is significantly low (~ 0.03). The model performance with respect to the salinity computation may be considered as “good” since the differences between the in situ and model salinity values at the surface are not greater than 2 units (Lewis & Allen, 2009). Both correlations (temperature and salinity) are statistically significant ($p_{\text{value}} < 0.0001$; 95% significance). The number of measurements and model outputs referred to specific temperature and salinity values (10-step range) is presented in Figures 4c and 4d, respectively. The range of values was divided in 10 equal steps, and the number of measured and simulated values of each step is included in the graphs. The salinity range between 36 and 37 revealed high occurrence frequencies, as derived from both model and measurements (350–400 records), while many records show values around 35 (~ 100). Both simulated and observed temperature fields agree with the high occurrence frequencies of the highest levels ($>28^\circ\text{C}$) and the low numbers of the values between 10 and 25°C .

The evaluation of the GoM-HYCOM 1/50 simulation against the DEEPEND observations highlighted very satisfactory model performance and supports the usage of simulated fields to investigate the evolution of the main offshore pathways of the brackish waters and their respective vertical structure.

3.2. Main Pathways of Riverine Waters

Three main episodes of offshore export of the northern GoM brackish waters were identified in July and August 2015, derived by model simulated and MODIS-derived SSS maps (Figures 5 and 6). We note that the satellite SSS fields are independent data (not assimilated in the GoM-HYCOM 1/50 simulations).

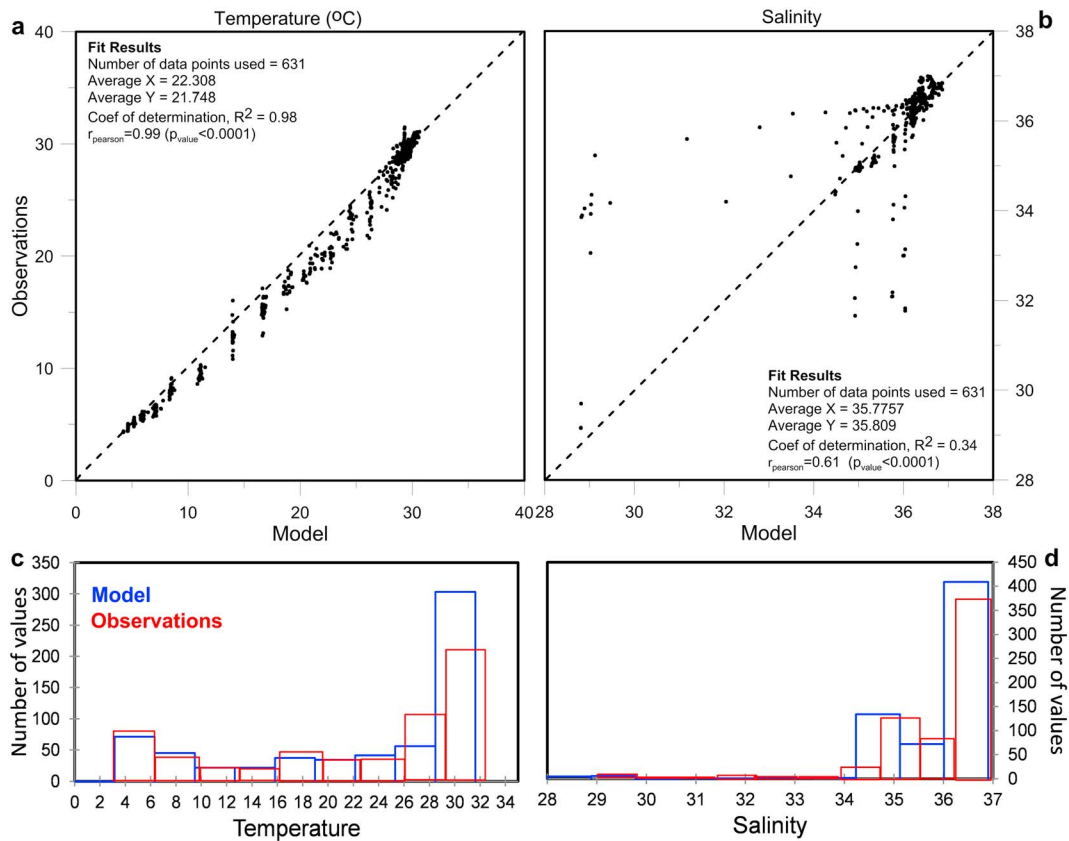


Figure 4. (a) Temperature and (b) salinity scatter diagrams of all observed and simulated pairs derived at DEEPEND locations (Figure 1a). The number of points used, the axis mean, the coefficient of determination (R^2), the Pearson coefficient (r_{pearson}), and the p_{value} for each case in (a) and (b) are presented. Number of (red) observed and (blue) simulated (c) temperature and (d) salinity values. The x axes in (c) and (d) represent the range of each parameter in a 10-step scale.

In June (Figure 5a), large quantities of low-salinity waters, resulting from elevated spring river runoffs, were advected along the western shelf (LATEX). The high discharge levels for all northern GoM rivers in spring (Table 1), in combination with the strong southeasterly winds from May until mid-June (Delta area and LATEX; Figure 7), enhanced the downstream westward currents of the MR plume, as expected from these conditions (Androulidakis et al., 2015, 2018; Androulidakis & Kourafalou, 2013; Kourafalou & Androulidakis, 2013; Schiller et al., 2011; Walker et al., 2005). Enhanced precipitation in this region during summer also contributes to lowering the surface salinity (Dinnel & Wiseman, 1986). The LATEX shelf experienced the largest precipitation of 2015 in late May (Figure 7; ECMWF precipitation superimposed on Buoy 42035 winds), and weaker but continuous rainfall also occurred during the second week of June. In late May and early June, the LC extension was south of 28°N , at some distance from the MR Delta. These four conditions (strong discharges, downwelling-favorable [southeasterly] winds, high precipitation rates, and LC system away from the MR Delta) favored the accumulation of low-salinity waters over the LATEX shelf during June 2015, in agreement with the satellite-derived SSS (Figure 5b) and chl-*a* concentrations (Figure 5d). The signal of low-salinity and high chl-*a* waters is apparent over the western part of the LATEX shelf, while it is completely absent over the central Gulf and very weak over the MAFLA shelf. No offshore export of brackish waters was detected under these conditions.

The formation of the strong downstream current in June was also confirmed by the slope of all coastal altimetry data over the LATEX shelf (section 2.1.2). The slope was calculated by dividing the altimetry differences between all X-TRACK coastal altimetry along-track points (DH) with the respective distances (DL). The mean values of the slope (DH/DL), derived from all successive points, are presented, for June and August, in Table 2. All available tracks around 10 June were within the coastal current region and revealed positive DH/DL values, indicating strong westward downstream geostrophic currents in accordance to the

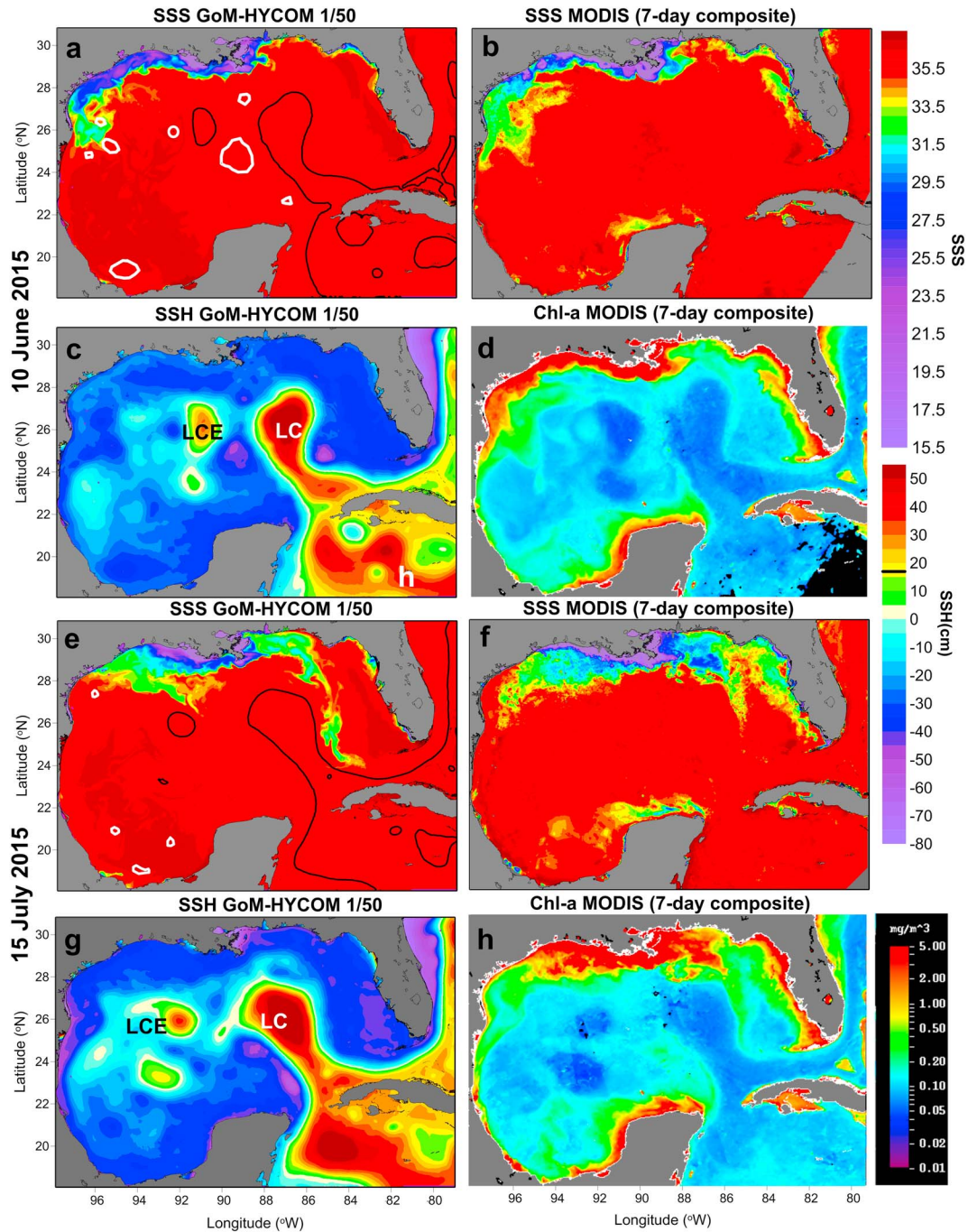


Figure 5. Horizontal distribution of (a and e) simulated SSS, (b and f) satellite SSS, (c and g) simulated SSH, and (d and h) satellite chl-*a* concentrations on 10 June (upper four panels) and 15 July (lower four panels) 2015. The chl-*a* concentrations and satellite SSS fields are composites over 7 days from MODIS/Aqua fields. The white (−35-cm contour; high negative SSH threshold to demonstrate only the major features) and black (17-cm contour; Leben, 2005) lines in the simulated SSS fields were derived as model SSH anomalies from the daily spatial mean over the GoM and mark the major cyclonic eddies and anticyclonic circulation features, respectively. Note that the low-salinity satellite values over the West Florida Shelf and Campeche Bank may contain large uncertainties due to algorithm artifacts. SSS = Sea Surface Salinity; SSH = Sea Surface Height; LC = Loop Current; LCE = Loop Current Eddy; GoM-HYCOM = Gulf of Mexico Hybrid Coordinate Ocean Model; MODIS = Moderate Resolution Imaging Spectroradiometer.

sea level setup solution (Csanady, 1984; Kourafalou, 2001). The evolution of the westward downstream currents over the westernmost part of the shelf at 97°W in mid-June, carrying low-salinity waters (Figures 5a and 5b), was also confirmed by the coastal altimetry data derived along the westernmost available satellite track (#52; Figure 1a), revealing relatively high positive slope (3.5×10^{-7} ; Table 2).

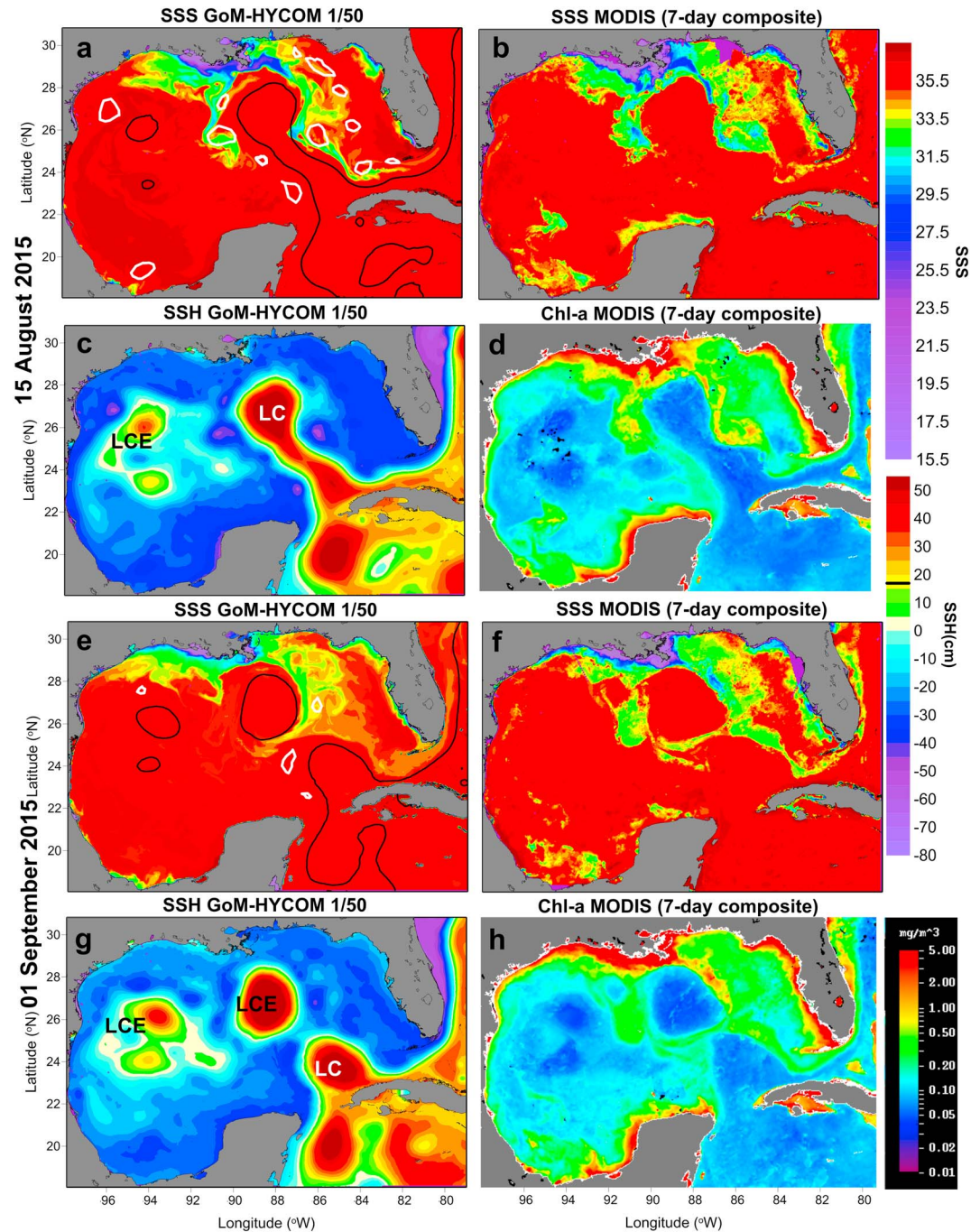


Figure 6. Same as Figure 5, for 15 August and 1 September 2015.

Almost 1 month later, in mid-July, an extensive low-salinity branch was formed along the eastern boundary of the LC (Figure 5e), carrying high chl-a waters toward the southeastern Gulf (Figure 5h). This eastern pathway was also confirmed by the respective satellite-derived SSS distribution (Figure 5f). Winds over the LATEX shelf (Buoy 42035) and especially over the Delta (Buoys SPL1 and 42040) and the MAFLA shelf (Buoy 42039) turned toward a prevailing eastward component in July (Figure 7). These wind conditions worked against the westward buoyancy-driven coastal current and, in combination with the low precipitation rates, reduced the accumulation of brackish waters over the LATEX shelf (Figures 5e and 5f). The upwelling-favorable westerly winds effectively blocked the westward

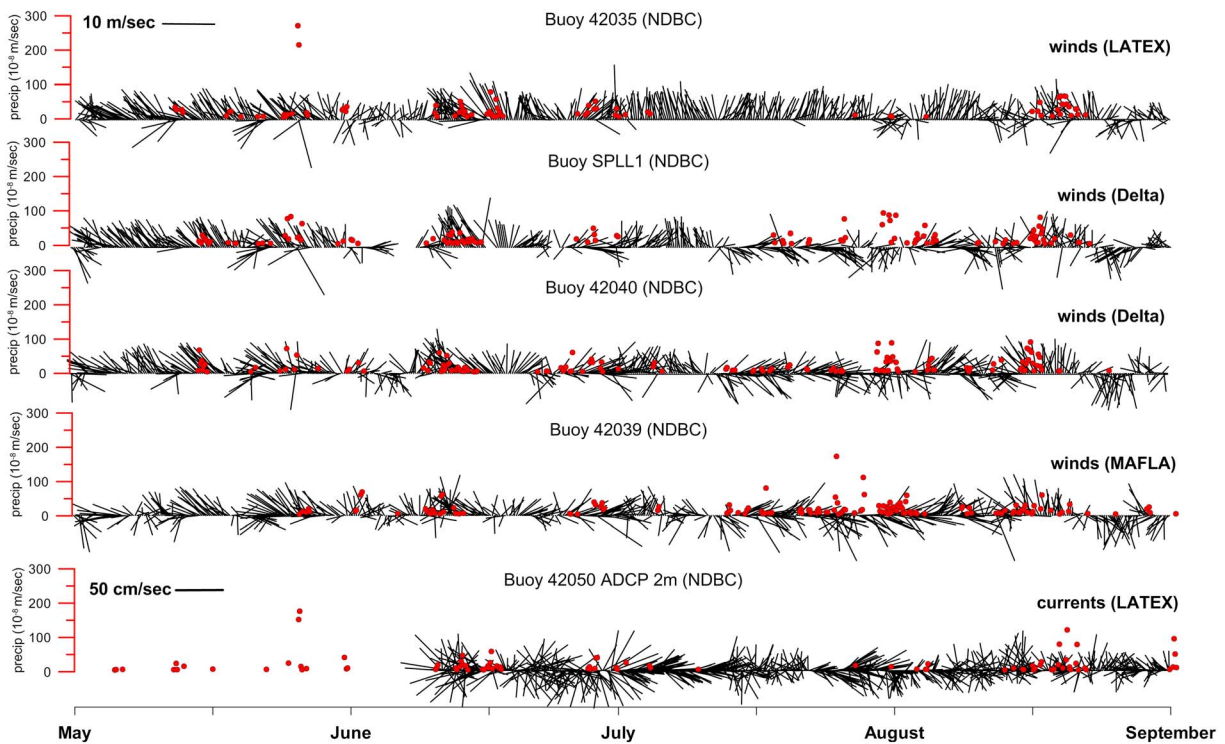


Figure 7. Time series of precipitation (red dots) rates (precip; 10^{-8} m/s), derived from 3-hourly European Centre for Medium-Range Weather Forecasts fields and superimposed over the respective wind vectors (m/s), measured by four NDBC buoys located at LATEX (42035), Mississippi Delta area (SPLL1 and 42040), and MAFLA (42039). The respective near-surface current vectors (cm/s) from the only available buoy at LATEX shelf (42050) are also presented. The locations of the five buoys are presented in Figure 1a. Only precipitation rates over 5×10^{-8} m/s are shown. All vectors are presented every five steps showing the direction toward the winds and currents are going. NDBC = National Data Buoy Center; LATEX = Louisiana-Texas; MAFLA = Mississippi-Alabama-Florida Shelf.

downstream current and enhanced the offshore spreading of the MR waters to the south of the Delta (as in Ortner et al., 1995; Walker et al., 2005; Schiller et al., 2011; Androulidakis et al., 2015) and over the MAFLA shelf (as in Le Hénaff & Kourafalou, 2016). Although the LC remained in a similar extension as in June (south of 28°N ; Figure 5g), the contribution of winds to the offshore spreading led to the formation of this first eastern branch in mid-July. Moreover, the LC Eddy (LCE) named Eddy Nautilus (Leung et al., 2016) propagated westward and closer to the LATEX shelf ($92^{\circ}\text{W}-26^{\circ}\text{N}$); the LCE was previously located west of the LC at $91^{\circ}\text{W}-26^{\circ}\text{N}$ in mid-June (Figure 5c). This led to the entrainment

of low-salinity waters over the northern periphery (26.5°N) of the LCE and to the further removal of brackish waters from the LATEX shelf, initializing the formation of a secondary western (with respect to the LC) offshore branch of low-salinity waters at $93^{\circ}\text{W}-27^{\circ}\text{N}$ that originated from the LATEX shelf (Figure 5e). The contribution of the LCE to the eastward spreading of the brackish waters over the shelf is discussed in section 4.1. The currents measured over the central LATEX were eastward (Buoy 42050; Figure 7) during the first 2 weeks of July. This is consistent, through the Ekman theory, with the southerly winds observed locally (Buoy 42035; Figure 7).

From late July to early August, the northern GoM rivers showed a peak in discharge ($>40,000 \text{ m}^3/\text{s}$; Figure 1b), releasing significant quantities of freshwater over the northern GoM shelf. The contribution of the MR, representing 70% of the total northern GoM river input, also showed a peak. Moreover, the precipitation rates were relatively high over the central-northern Gulf (Buoys SPL11, 42040 and 42039; Figure 7), while westerly winds prevailed over all areas during most of August (except at

Table 2
DH/DL ($\times 10^{-7}$) Ratio (Slope) From #052, #117, #128, and #193 Satellite Tracks During Two Types Opposite Coastal Currents Over Louisiana-Texas Shelf in June and August

Satellite track	June (westward current) DH/DL (date)	August (eastward current) DH/DL (date)
052	3.5 (16 June)	-8.4 (15 August)
117	2.4 (9 June)	-1.2 (17 August)
128	1.5 (9 June)	-2.6 (18 August)
193	4.0 (12 June)	-1.0 (20 August)

Note. DH expresses the mean Sea Level Anomaly differences of all along-track points located between the coast and offshore at 28°N (Figure 1a), based on the X-TRACK coastal altimetry data. DL is the distance between the points along each satellite track (approximately 0.05°). Positive (negative) values lead to westward (eastward) geostrophic current. The exact date of each available satellite track over Louisiana-Texas is also presented.

Buoy 42035, where they were mostly southerlies). Eddy Nautilus propagated further to the west, forming anticyclonic currents (eastward) closer to the LATEX shelf and contributing to the formation of an extensive western branch of low-salinity waters at 92°W in mid-August (Figures 6a–6c; see also section 4.1 for the regional effects). Simultaneously, the LC extended further northward and formed a second eastern branch, which was apparent in the maps of model SSS (Figure 6a), MODIS-derived SSS (Figure 6b), and chl-*a* composites (Figure 6d). The eastern branch reached the Florida Keys, while the western branch was also significantly extended southward, bringing low-salinity waters over the central Gulf to about 24°N. The surface chl-*a* concentrations in both pathways reached the level of 2 mg/m³ even in remote areas far from the northern Gulf. Although the river discharges were low in mid-August, the regional ocean conditions, in tandem with favorable winds, contributed to the formation of these parallel offshore pathways in agreement with findings by Le Hénaff and Kourafalou (2016). The weakening of the downstream westward current along the LATEX shelf, supported by both simulated and satellite SSS and chl-*a* fields, was also confirmed by the negative coastal altimetry slopes indicating eastward geostrophic currents in August, in contrast to June's positive slopes (Table 2). Several LCFEs were detected around the LC during its extended phase toward the northern Gulf (Figure 6c); the larger ones are superimposed with white lines in the model salinity map (Figure 6a), and their effects on the evolution of the brackish branches are discussed in section 4.1. The sources of the brackish waters along these two pathways (rivers and/or rainfall) may have significant biochemical implications and are discussed in section 4.3. Finally, in late August, a second LCE, namely, Eddy Olympus (Leung et al., 2016), was released from the LC (Figure 6g). This eddy shedding and the LC withdrawal to the south of 24°N interrupted the connectivity between the northern and southern parts of the GoM. The eastern branch was entrained around Eddy Olympus, carrying brackish waters to the west over the central Gulf (Figures 6e and 6f).

In the beginning of summer 2015 (June), no offshore export of riverine waters was detected. Low-salinity waters covered the northwestern GoM shelves, under the strong downstream currents from the MR Delta, high discharge rates of the LATEX rivers, prevailing easterly winds, and strong rainfall over the shelf areas. During the following months (July and August), we identified three episodes of extensive offshore export of low-salinity waters that initially originated in the northern GoM, along two major pathways, east and west of the LC.

4. Discussion

We examine the effects of the regional circulation, such as the LC and the mesoscale eddies (LCEs and the LCFEs), on the dynamics of the western and eastern offshore pathways (section 4.1) and especially on the characteristics of their vertical structure and stratification around the period of in situ surveys in August 2015 (section 4.2). In addition to the realistic GoM-HYCOM 1/50 simulation (hereafter referred to as *Realistic*), we have used two idealized simulations (*NoMR* and *NoMR/NoPrecip* experiments), presented in section 2.2, to investigate the origin of the brackish waters along those two pathways and over remote areas, such as the Straits of Florida (section 4.3).

4.1. Regional Circulation Effects on the Evolution of the Offshore Branches of Low-Salinity Waters

We first examine the offshore (southward) branch along the western side of the LC. This branch was formed between Eddy Nautilus on its west side and two successive LCFEs on its east side in mid-August (27°N and 25.5°N; Figure 6a). In order to describe the prevailing conditions that contributed to the formation of the western branch, we examined the wind and LCE evolution over the northwestern Gulf. The LCE was located around 91°W in mid-June, away from the low-salinity plume (35 isohaline) that was mainly extended over the inner shallower part of the LATEX shelf (north of the 50-m isobath; Figure 8a) and deeper offshore of the 1,000-m isobath at the western part of the shelf (west of 95°W; Figure 8a). The high and low offshore SSH values are associated with the anticyclonic and cyclonic features (LCE and LCFE eddies, respectively). Northward currents prevailed over the entire shelf from the coast to the shelf-break area as far as the 1,000-m isobath in mid-June (Figure 8a) due to the prevailing southeasterly winds (Figure 7). However, near-surface slope currents were strongly eastward by early August, as the LCE extended over a vast area along the LATEX shelf-slope (1,000- to 200-m isobaths) between 96°W and 91°W. The area of separation between the LCE and the LC had been broadened, as a strong LCFE intruded from the south (it can be

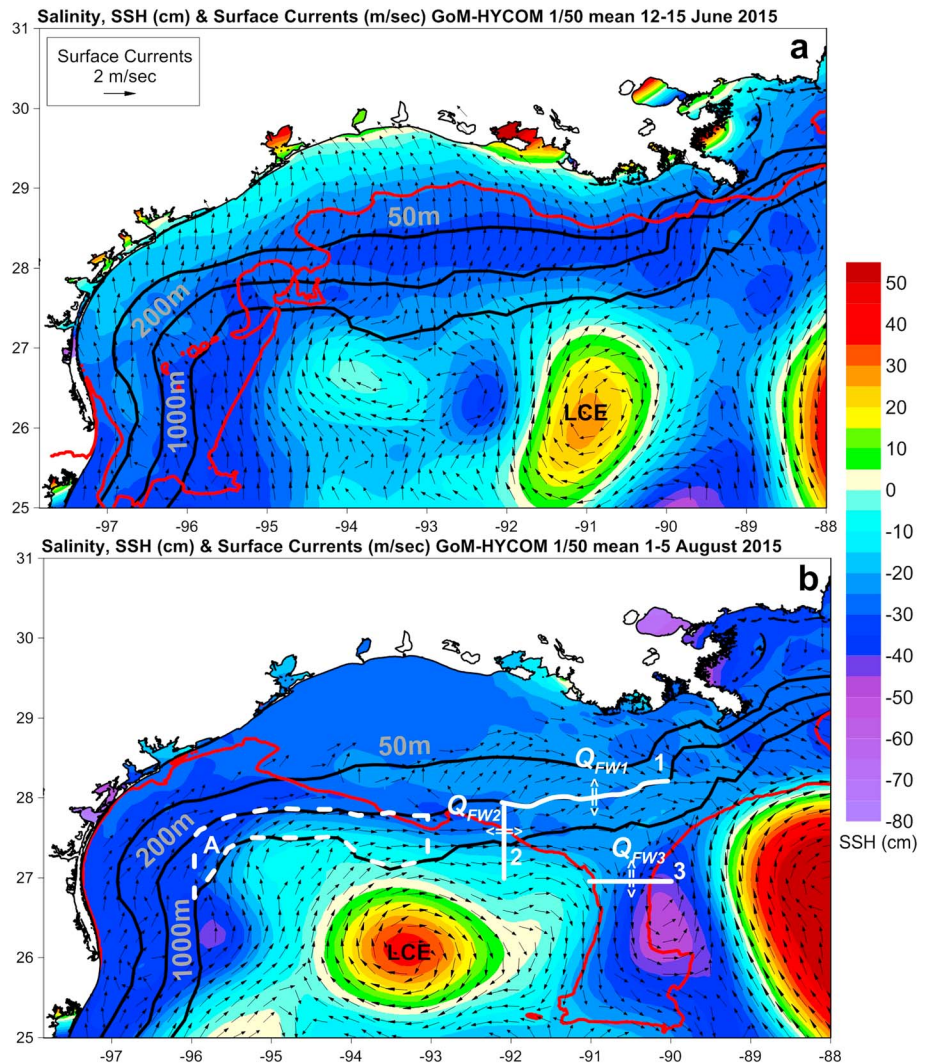


Figure 8. SSH (cm) and surface currents (m/s) over the northwestern Gulf, derived from the GoM-HYCOM simulations and averaged (a) from 12 to 15 June and (b) from 1 to 5 August 2015. The red line indicates the respective mean 35 isohaline. The black lines indicate the 50-, 200-, and 1,000-m isobaths (numbers in gray letters). The dashed white lines mark the Area A used to compute the Relative Vorticity normalized by the Coriolis frequency (RV/f). The solid white lines show the Sections 1–3 of the time series presented in Figure 9. GoM-HYCOM = Gulf of Mexico Hybrid Coordinate Ocean Model; SSH = Sea Surface Height.

seen at 27°N on Figure 8b). The dipole of these counterrotating eddies (LCE and LCFE) was in close proximity to large amounts of plume waters near the shelf-break. Fournier et al. (2016), based on satellite data, showed that 2015 was a major flooding year, when the freshwater plume extended over the shelf and was carried along the Texas coast by coastal currents during June–July, in agreement with the plume pattern presented Figure 8a. Then the plume was advected offshore in August by the currents of an anticyclonic eddy (Eddy Nautilus) that was shed off the extended LC earlier in the year (Figure 8b). Thus, we had three necessary conditions for offshore advection of MR plume waters (strong discharge in late July, westerly winds, and offshore circulation in close proximity to plume waters), in agreement with earlier studies (as by Ortner et al., 1995). In addition, we had counterrotating offshore flows (LCE and LCFE) that created the western branch as an offshore (southward) jet, a necessary near-field condition that has been discussed by Schiller et al. (2011). The distribution of the 35 isohaline, derived from the GoM-HYCOM 1/50 simulation, illustrates the offshore transport of the brackish waters and their southward spreading between the LCE and the LCFE at 91–90°W (Figure 8b). We now investigate the

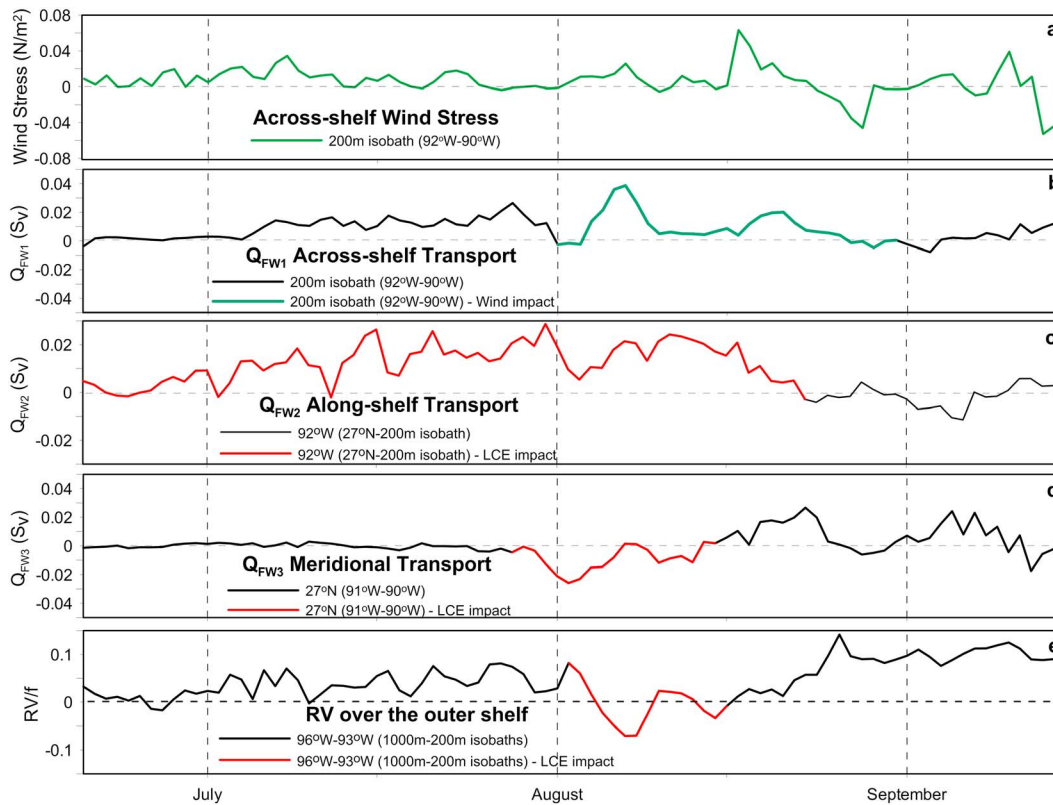


Figure 9. Time series of daily (a) across-shelf (meridional) wind stresses derived from the European Centre for Medium-Range Weather Forecasts fields and averaged along the 200-m isobath, between 92°W and 90°W, (Section 1; Figure 8b) from 20 June to 15 September 2015. Positive (negative) values represent northward (southward) direction of the wind. (b) Across-shelf transport of freshwater (Q_{FW1}) averaged over the same section derived from the Gulf of Mexico Hybrid Coordinate Ocean Model 1/50 simulations. (c) Along-shelf (zonal) transport of freshwater (Q_{FW2}) averaged at 92°W, between 27°N and the 200-m isobath (Section 2; Figure 8b). (d) Meridional transport of freshwater (Q_{FW3}) across the 91–90°W section (Section 3; Figure 8b). Positive (negative) values represent onshore (offshore) and eastward (westward) transport of freshwater. (e) Time series of Relative Vorticity normalized by the Coriolis frequency (RV/f) averaged over the Area A located between 96°W and 93°W and between the 1,000- and 2,000- isobaths (marked in Figure 8b). The green and red lines in the transport and RV/f time series indicate the periods of prevailing effects on transport caused by the wind and by the LCE, respectively. LCE = Loop Current Eddy.

main processes that supplied brackish waters to the area between the LCE and LCFE and quantify the related transport.

The computation of the integrated freshwater transport Q_{FW} through a section, based on Schiller et al. (2011), is given by

$$Q_{FW} = \int \int_{-h}^{\eta} fw_f V dz dx,$$

where V is the horizontal velocity normal to the section, η is the sea level, and h is the bottom depth and the integral with respect to x , which is the horizontal distance along the section; all parameters are derived from the *Realistic* simulation. The freshwater fraction fw_f is equal to $fw_f = \frac{S_b - S}{S_b}$, where S is the salinity from the *Realistic* simulation and S_b is the background salinity without the effect of the river discharge and precipitation input; S_b was obtained from the twin *NoMR/NoPrecip* experiment. Figure 9 presents time series of freshwater transport through the three sections marked in Figure 8b. The across-shelf (north-south) transport (Q_{FW1}) is computed at the 200 m Section 1 (Figure 9b) and is accompanied by the wind stress time series across the same section (Figure 9a). The wind effect dominates the transport during the first days of August and between 15 and 20 August, when both time series show positive (northward peaks).

Strong eastward transport of freshwater was computed across Section 2 (Q_{FW2} ; Figure 9c) over the outer shelf in July and August, when the LCE was present along the shelf-slope. In early August, the LCE affected the entire region between the 1,000- and 200-m isobaths between 96°W and 93°W (Figure 8b), inducing

eastward anticyclonic currents with negative vorticity values (Relative Vorticity with respect to the Coriolis frequency; RV/f in Figure 9e). The western region of the outer shelf that was previously dominated by low-salinity waters in mid-June (Figure 8a) was characterized by eastward currents and higher salinities in early August (Figure 8b). The LCE impact supported the eastward transport of freshwater south of the 200-m isobath (Q_{FW2}), supplying the area between the LCE and LCFE with brackish waters. Oey (1995) and Nowlin et al. (2005) showed that the evolution of the LCEs near the western LATEX shelf may cause flow convergence in the southwestern shelf and produce eastward currents along the shelf-break. This was the case in August 2015, as the LCE was extended westward over the shelf-slope, in close vicinity to brackish waters that had been advected there under wind influence during the previous period. In addition, we had the presence of the cyclonic LCFE and the subsequent formation of the offshore (southward) jet that marked the start of the western branch between the two eddies. The Q_{FW3} freshwater transport across the 91–90°W section (Figure 8b) is almost zero or positive (e.g., late August) during the entire period, except during the western pathway formation in early August (Figure 9d). The strong negative (southward) freshwater transport supports the synergy of the counterrotating currents over the northern part of the western pathway. Our findings thus suggest that the influence of the LCE on the LATEX outer shelf is crucial for the formation of the western pathway because (1) the anticyclonic currents along its northern periphery supply brackish waters from the outer shelf directly to the central region and (2) the anticyclonic currents along its eastern periphery, in tandem with cyclonic eddies, may form strong offshore jets toward the south.

The eastern branch on 15 August 2015 was formed between the eastern LC boundary, characterized by strong southward currents, and a series of LCFEs located along the eastern side of the branch (Figure 10a). This pathway has been studied more extensively than the western pathway, and it has been connected to the offshore advection of nutrients and pollutants that can reach as far south as the Florida Straits. For instance, Androulidakis et al. (2018), based on a multiplatform observational study, showed that such pathways of waters of high chl-*a* concentrations might also carry pollutants such as oil patches that originated from around the MR Delta. Here we concentrate on the three-dimensional characteristics of both eastern and western pathways to advance the understanding of the processes that control the southward advection of riverine waters and associated materials.

We have marked 12 characteristic positions (1–12) to trace the far-field transports along the western and eastern pathways. The deepest plume away from the Delta was formed at Locations 9–11, along the eastern branch (20 m; Figure 10c). Locations 9–11 form an area where the LC follows a sharp curvature around a cyclonic LCFE (Figure 10a), allowing the entrapment of large quantities of brackish waters in the upper 20 m. The brackish plume was shallower south of 25°N. Similarly, the deepest plume along the western branch was formed at Locations 4–6, where a LCFE also evolved (~14 m; Figures 10a and 10b).

We calculated the daily transport of the brackish waters (Figure 10d) to quantify the transport rates, as well as the RV/f (Figure 11a) and Eddy Kinetic Energy (EKE; Figure 11b) distributions to recognize the eddy characteristics at different locations along the offshore branches. The negative transport rates during July and August across the 25.5°N sections (Figure 10d) indicate the evolution of the southward pathways of brackish waters. The first eastern branch in mid-July was the strongest of the entire summer (0.7 S_v), while a respective southward transport also detected along both eastern and western pathways in mid-August (0.4 S_v). The RV/f values along west and east of each pathway have opposite signs (Figure 11a). The anticyclonic LC and LCE patterns with negative vorticity and the cyclonic LCFEs with positive vorticity contribute to the southward propagation of the surface waters forming both branches. The highest positive RV/f along the branches were detected at Locations 2–4 for the western branch and Locations 9–12 for the eastern branch. The former (2–4) was between two LCFEs and Eddy Nautilus, and the latter (9–12) was located between two LCFEs and the LC. The computed EKE revealed high peaks in areas between the LC and the LCFEs, such as Locations 9–12. The northern parts of the eastern branch (e.g., Location 8) exhibited lower RV/f and EKE values due to the larger distance between the neighboring LCFE (~84.5°W) and the LC. Relatively high EKE areas along the western branch were also apparent between a LCFE and Eddy Nautilus (2–3). Outside the brackish branches, other areas with higher EKE values were also detected at 88.5°W–24.5°N and 86.5°W–23°N, in areas under the influence of LCFEs (Figure 11b).

The lowest SSS values (<30) and the deepest river plume (defined by the 35 isohaline) were shown, as expected, over the northern shelves and close to the MR Delta (>28°N; Figure 12c), where the low-salinity

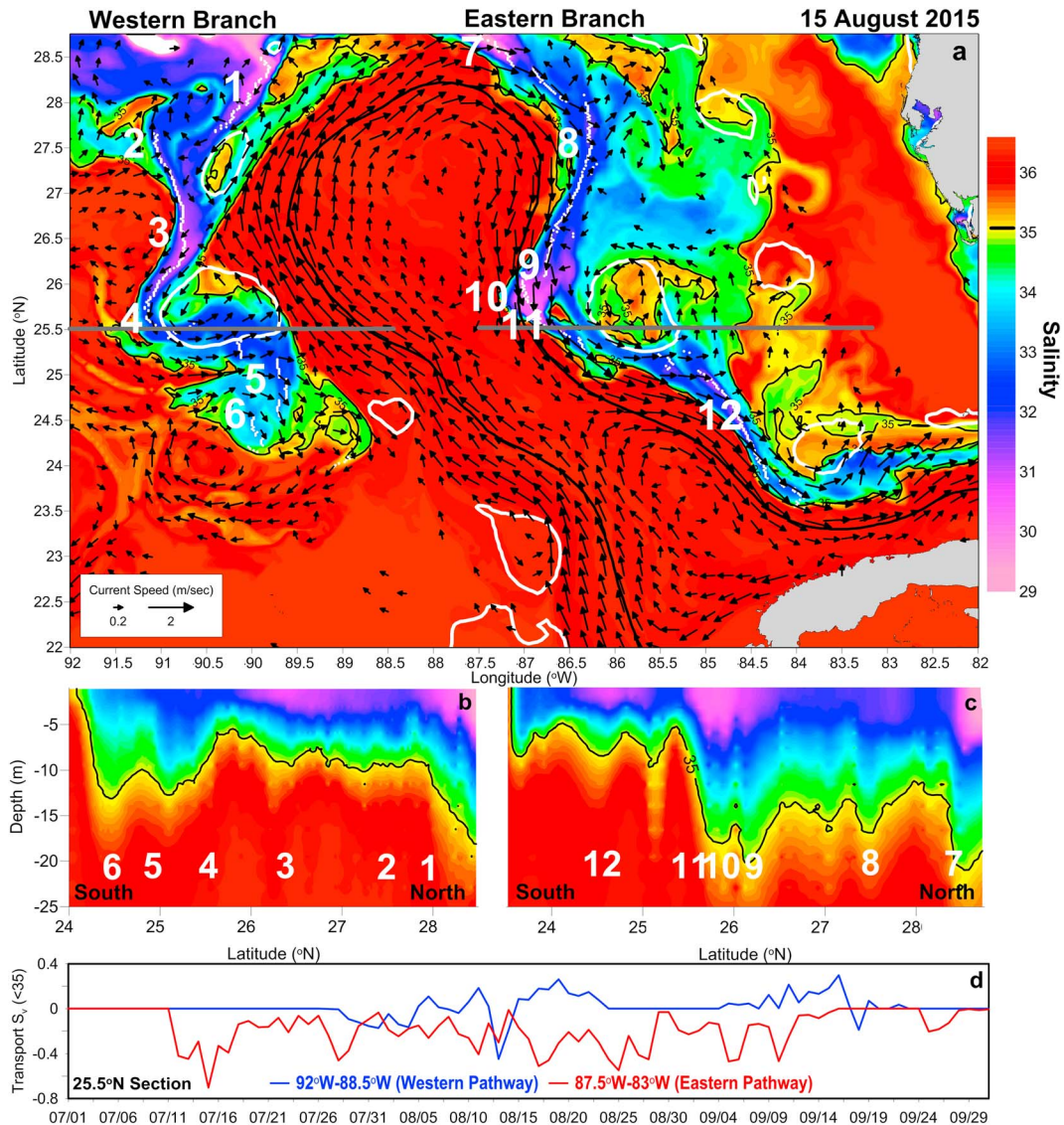


Figure 10. (a) Distribution of simulated near-surface currents (m/s) and Sea Surface Salinity over the western and eastern branches of brackish waters as derived from the Gulf of Mexico Hybrid Coordinate Ocean Model 1/50 simulation on 15 August 2015. Thick white and black lines indicate the Loop Current Frontal Eddies and the Loop Current, respectively. Only currents with speed larger than 0.2 m/s are shown. (b, c) Vertical salinity structure over the upper 25 m along the (b) western and (c) eastern branches that are indicated with white dots in (a). The 35 salinity contour is marked with a black thin line. (a–c) Twelve characteristic locations along the two branches are highlighted in both horizontal and vertical distributions. (d) Simulated daily transport (S_v) of the low-salinity (<35) waters across two zonal sections (92–88.5°W: Western Pathway; 87.5–83°W: Eastern Pathway) at 25.5°N, marked with gray lines in (a), from July to September 2015.

water masses accumulate in large quantities (within a thick layer deeper than 30 m; Figure 12e). The lowest mean SSS levels of the area around the MR Delta occurred at the end of July in agreement with the MR discharge peak ($>30,000 \text{ m}^3/\text{s}$; Figure 12a). As expected, the correlation between the SSS and river outflow was high ($R_{\text{Pearson}} > 0.65$; Figure 12a) over this area. Very low-salinity surface waters (<30) were advected by strong anticyclonic currents (1.5–2 m/s) at the northern tip of the LC and then spread eastward, reaching 87°W (Figure 12c), an area between the LC and a LCFE (Figure 10a). The simulated plume depth over this area agrees with the depth measured at the northernmost DP18 station (Figure 3e).

The brackish plume reached its thinner thickness inside the Straits of Florida at 84.25°W (~6 m), where it still extended down to ~10 m around 83°W (Figure 12f). The mean SSS values over the Straits of Florida dropped below 35.5 in mid-August, approximately 2 weeks after the northern region (Figures 12a and 12b); the low precipitation rates over the Straits suggest that this reduction can only be related to river waters

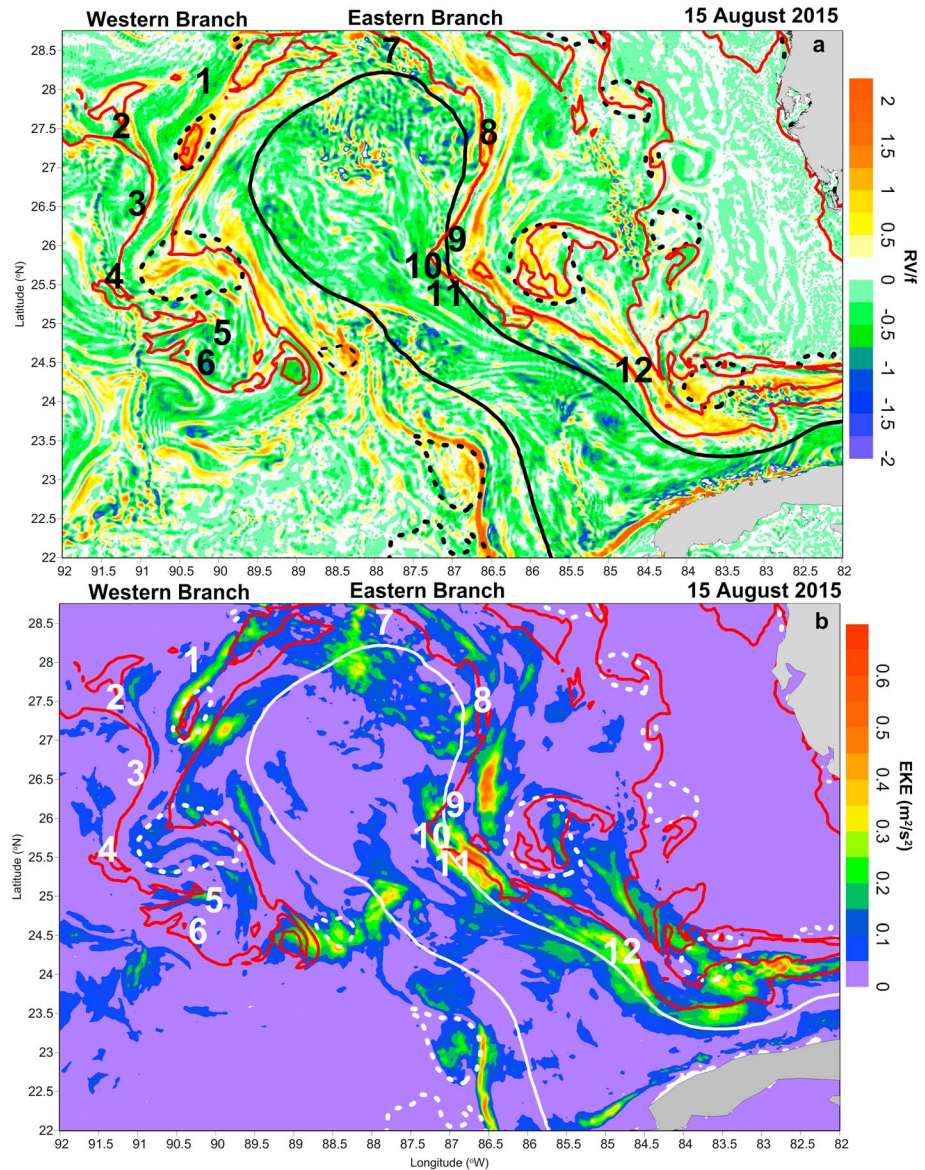


Figure 11. Distribution of (a) normalized Relative Vorticity with the Coriolis frequency (RV/f) and (b) EKE over the western and eastern branches of brackish waters as derived from the Gulf of Mexico Hybrid Coordinate Ocean Model 1/50 simulation on 15 August 2015. Dashed and solid black (a) and white (b) lines indicate the Loop Current Frontal Eddies and Loop Current, respectively. The 35 salinity contour is marked with a red solid line. Twelve characteristic locations along the two branches are marked (same locations as in Figure 10). EKE = Eddy Kinetic Energy.

from the North (see section 4.3). A cyclonic eddy was formed inside the Straits, contributing to a curvature of the FC between $84^{\circ}W$ and $83^{\circ}W$ (Figure 12d). Kourafalou and Kang (2012) showed that the cyclonic eddies along the southwest Florida shelf-slope interact with the FC and influence its meandering along the Straits. The brackish plume is elongated between the eastward southern part of the cyclonic eddy and the eastward FC, forming a clear west-east patch of low-salinity waters along the northern Straits ($24^{\circ}N$). The EKE was high between the cyclone and the FC (Figure 11b) over an area where the low-salinity branch evolved around the cyclone, resulting considerably larger thickness (~ 10 m; Figure 12f). We conclude that the presence of cyclonic eddies along the LC/FC system is associated with the thickness and decreased salinity of the brackish branch in the central Gulf and along the Straits of Florida. We investigate further using glider data collected along the LC during August 2015.

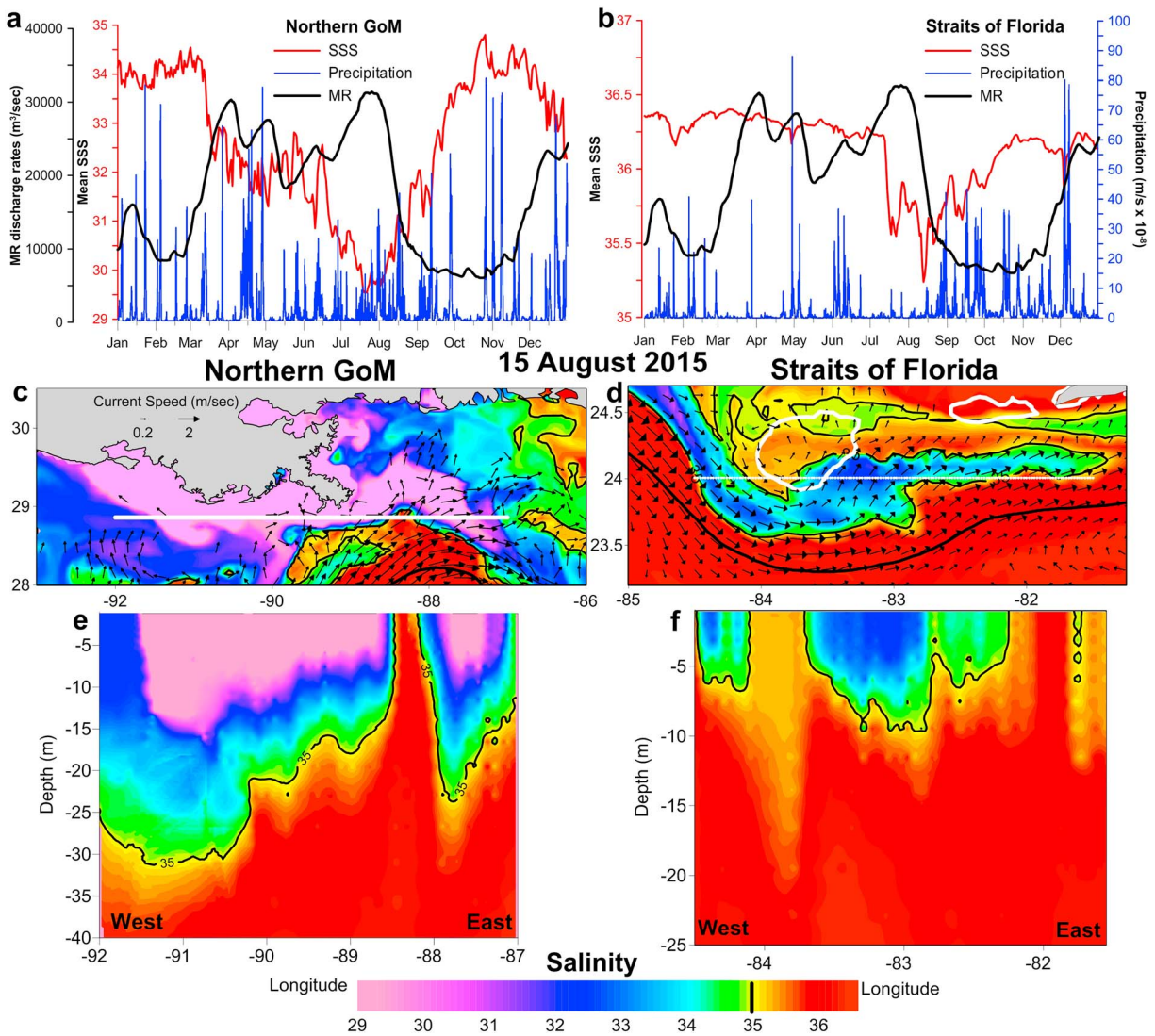


Figure 12. Daily MR discharge rates (m^3/s , black line), SSS (red line; GoM Hybrid Coordinate Ocean Model 1/50), and 3-hourly precipitation ($\text{m/s} \times 10^{-8}$, blue line; European Centre for Medium-Range Weather Forecasts), averaged over the (a) northern GoM and (b) Straits of Florida in 2015. Distribution of near-surface currents (m/s) and SSS over the (c) northern GoM and (d) Straits of Florida as derived from the GoM Hybrid Coordinate Ocean Model 1/50 simulation on 15 August 2015. Only currents with speed larger than 0.2 m/s are shown. Simulated computed vertical salinity structure over (e) northern GoM (upper 40 m) and (f) Straits of Florida (upper 25 m), indicated with white lines in (c) and (d), respectively. The 35 salinity contour is marked with a thin black line. GoM = Gulf of Mexico; SSS = Sea Surface Salinity; MR = Mississippi River.

The Slocum glider, deployed at the northwestern extension of the LC on 9 August 2015, followed the anticyclonic southward rotation of the LC until 22 August, similar to the eastern branch (Figure 13). The glider moved very close but outside of the eastern branch, along an inner LC front, until 87°W – 26°N , measuring high salinity values (>36) in both surface layers (Figure 13b) and at depth (Figure 13e). It crossed the eastern branch east of 86.8°W and was entrapped in the LCFE that participated in the LCE shedding at the end of August (Figure 13c). Low-salinity waters also followed a similar path inside the cyclone; observed (Figure 13e) and simulated (Figure 13d) surface data confirm the existence of low-salinity water masses inside the cyclone. The observed plume thickness was around 20 m (Figure 13e), in agreement with the depth derived from the simulated fields over this part of the branch (Figure 10c). This cyclonic eddy was also confirmed through the upwelling of relatively low temperature ($<26^\circ\text{C}$) waters measured by the glider between 50- and 100-m depth (east of 87°W ; Figure 13f); higher temperature ($>27^\circ\text{C}$) was measured over the upper 100 m along the glider's track before its entrapment in the eddy. The glider also provided

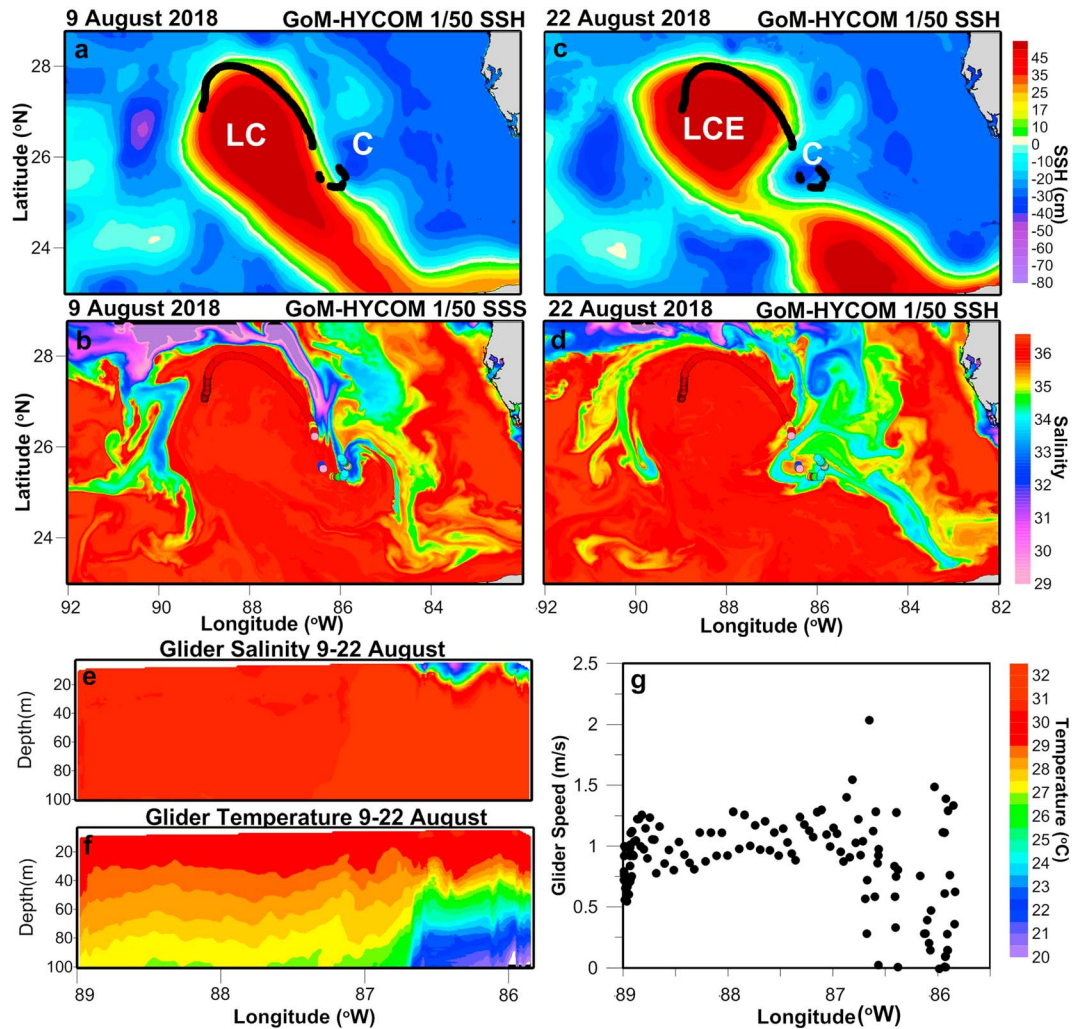


Figure 13. Horizontal distribution of simulated (GoM-HYCOM 1/50 model) SSH (a and c) and SSS (b and d) on 9 and 22 August 2015. The glider trajectory from 9 until 22 August 2015 is marked with black dots on the SSH fields and with respective colored dots of the measured SSS on the SSS fields. The LC, the LCE, and the C are also marked on the SSH maps. Vertical structure of (e) salinity and (f) temperature (glider data) over the upper 100 m along the glider's trajectory. (g) Glider speed (m/s) along its trajectory. GoM-HYCOM = Gulf of Mexico Hybrid Coordinate Ocean Model; LC = Loop Current; LCE = LC Eddy; C = Loop Current Frontal Eddy; SSH = Sea Surface Height; SSS = Sea Surface Salinity.

information about the current speeds along the LC and inside the LCFE. The glider's speed was relatively high during its displacement along the LC, with lower values (0.5–1 m/s) during the first days (~89°W) and its northward pathway (Figure 13g). The speed increased after its southward turn and ranged above 1 m/s until the glider's interaction with the LCFE, at which point it increased up to 2 m/s in the western side of the eddy, in agreement with the simulated strong currents presented in Figure 10a. However, the speed rapidly decreased after its anticlockwise loop inside the LCFE at the end of its mission (<0.5 m/s). This result also agrees with the EKE fields, which showed larger values over the western side of the LCFE (9–11 locations in Figure 11b) and smaller values in the areas away from the LC boundary such as the eastern side of the cyclone. The data suggest that the strong currents associated with the LC increased the propagation speed of the low-salinity waters along the branches. In contrast, the entrainment of the brackish waters inside a cyclonic eddy seems to slow down the speed, thus delaying its southward propagation. This evolution of the brackish waters under the influence of the mesoscale cyclonic eddies is also depicted in the transport rates (Figure 10d) in mid-August, when both eastern and western transports were half of the transport of the eastern branch in mid-July (without LCFE effects).

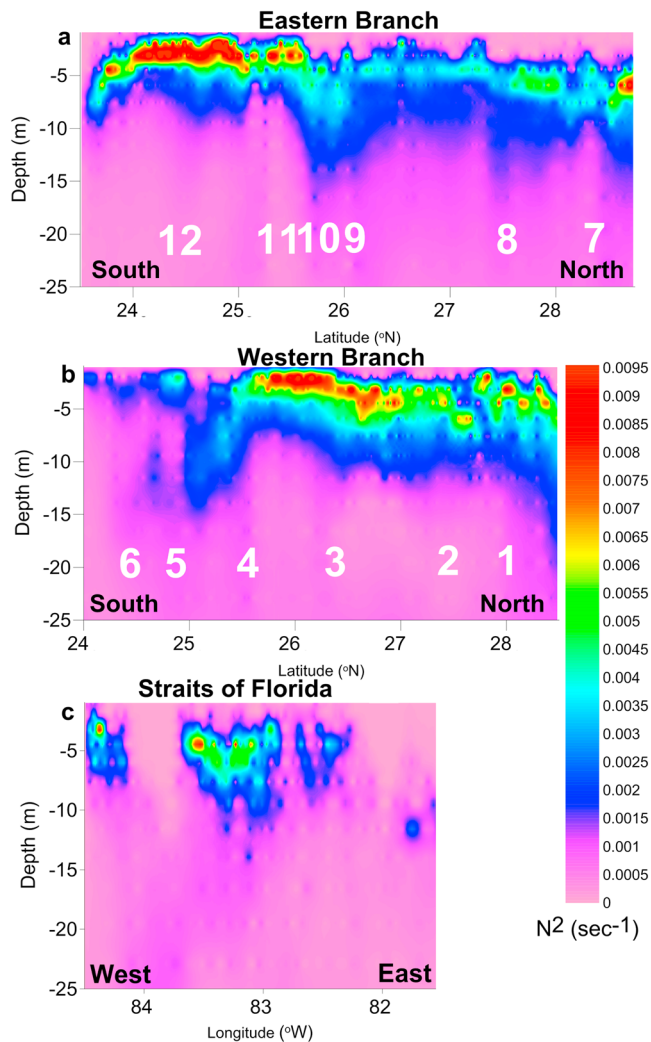


Figure 14. Vertical distribution of Brunt Väisälä frequency N^2 (s^{-1}) over the upper 25 m along (a) the eastern branch, (b) the western branch, and (c) the Straits of Florida as derived from the Gulf of Mexico Hybrid Coordinate Ocean Model 1/50 simulation on 15 August 2015. The branch pathways are marked in Figures 10 and 11. The Straits of Florida section is marked in Figure 12. Twelve characteristic locations along the two branches are marked (same locations as in Figures 10 and 11).

was characterized by lower stratification frequencies, concentrated again around the depth of 5 m (Figure 14c), in agreement with the *MLD* distribution that revealed shallow mixed layers (0–5 m) along the Straits (Figure 15c). We note that a homogenous water column with almost zero N^2 appeared at 84°W (Figure 14c), outside of the brackish plume (Figure 12d).

The central part of the western branch (Locations 2–4; Figure 14b) was characterized by strong N^2 frequencies ($>0.007 s^{-1}$). This area was located between two cyclonic LCFEs to the east and Eddy Nautilus to the west (Figure 6c); the accumulation of brackish waters north of the LCFE in Location 4 (Figure 10a) reduced the SSS levels (upper 5 m; Figure 10b) and increased the respective Brunt-Väisälä frequency (Figure 14b). The strongest brackish signal in both salinity and N^2 distribution was detected over the upper 10 m and especially over the upper 5 m ($0.009 s^{-1}$), in agreement with the mixed layer estimate (Figure 15). South of Location 4, the branch rotated cyclonically around the LCFE (Figure 10a), reducing the stratification frequencies ($0.002 s^{-1}$) but extending the plume signal at depth (down to 15 m; Figure 14b), similar to the eastern branch.

4.2. Vertical Structure of the Offshore Low-Salinity Pathways

The Brunt-Väisälä stratification frequency N^2 was computed (Figure 14) from the simulated fields along the brackish plumes on 15 August 2015 (Figures 10 and 12). The depth where the Brunt-Väisälä frequency reveals higher peaks in thin vertical thicknesses is associated with the existence of strong pycnoclines. In both branches, the highest values occurred over the upper 5 m, due to the accumulation of very low-salinity waters above saltier waters influenced by the deeper open ocean. The *MLD* distribution, based on a variable sigma- t (σ_t) criterion (Felton et al., 2014), supports the formation of strong pycnoclines at those depth levels (0–5 m) along the branches in all study events (Figure 15). Shallow *MLDs* were detected only around the MR Delta and over the LATEX shelf on 10 June, when the offshore brackish branches were totally absent and the mixed layer over the central Gulf was determined by other thermohaline factors (Figure 15a). During the formation of the three branches (one in mid-July and two in August), mixed layers shallower than 5 m were detected in remote areas along the pathways. Although the signal of the brackish waters may extend to deeper layers, as presented in section 4.1, the base of the mixed layer and the respective highest Brunt-Väisälä frequencies were at the shallow upper layer, closer to the surface, increasing the ability of the surface low-salinity waters to move offshore (Morey et al., 2003). The signal of the brackish waters was also evident in the stratification distribution (Figure 14) over similar depths as in the salinity vertical distribution (Figures 10 and 12).

The highest values of N^2 ($>0.007 s^{-1}$) were observed over the southern part of the eastern branch ($<25.5^\circ N$; Figure 14a). Weaker stratification was detected over a thicker vertical layer (5–20 m) in the area between the LCFE and the LC curvature (Locations 9–11; Figure 14a). Although the N^2 frequency revealed lower values over this layer (0.0015 – $0.0035 s^{-1}$), indicating the absence of a strong pycnocline in comparison with the southern part of the branch, the presence of a LCFE along the LC appears to be associated with spreading the low-salinity waters toward deeper levels, extending the vertical influence of the brackish waters in the central GoM. This area presented a 10-m surface layer of very low-salinity waters, while its signal was also apparent down to 20 m (Figure 10c). No strong pycnocline was observed along that branch north of 26°N, except for a region very close to the Delta (north of Location 7), where high Brunt-Väisälä frequency was computed at approximately 7 m. The southern part of the eastern branch, inside the Straits of Florida,

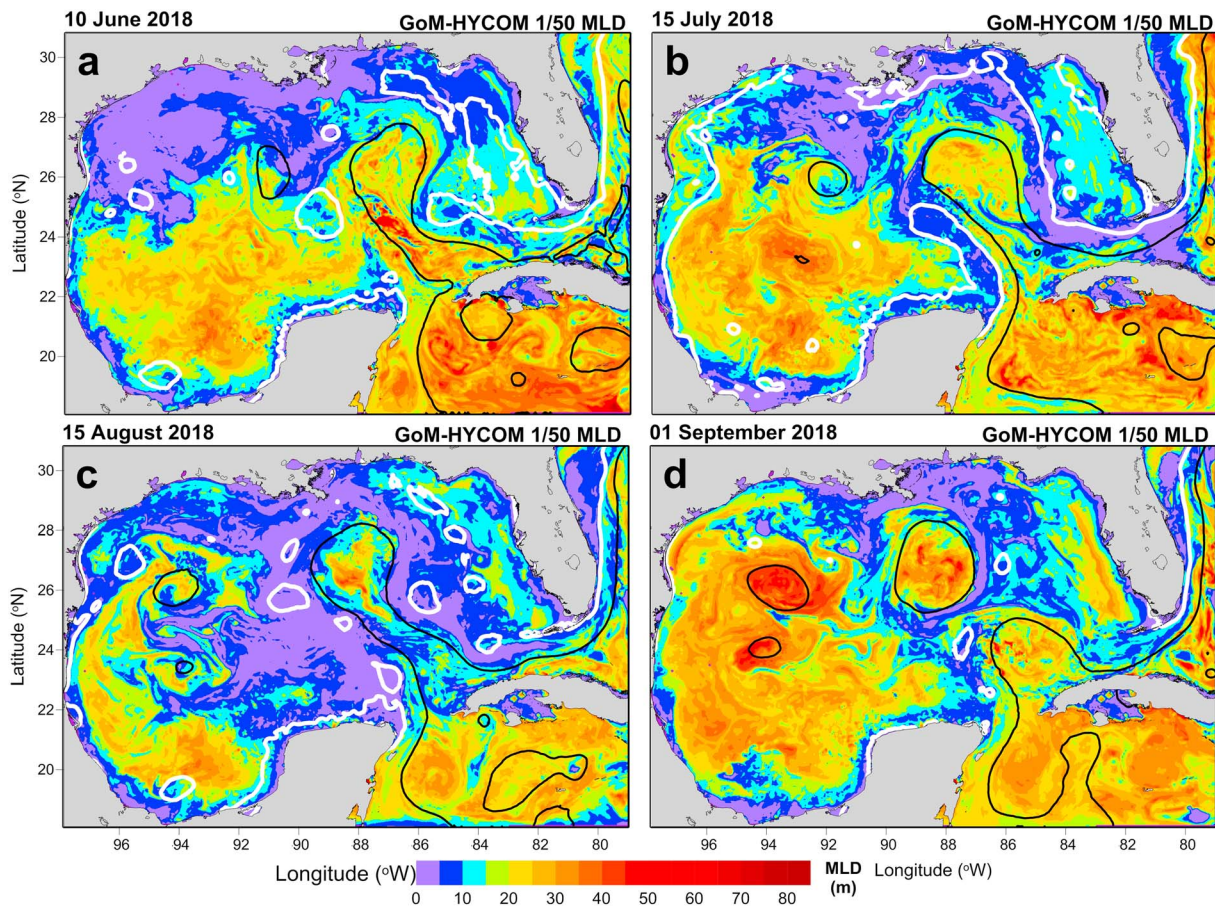


Figure 15. Horizontal distribution of *MLD* (m), derived from the GoM-HYCOM 1/50 simulation, on (a) 10 June, (b) 15 July, (c) 15 August, and (d) 1 September. The white (−35-cm Sea Surface Height anomaly contour) and black (17-cm Sea Surface Height anomaly contour) lines mark the major cyclonic and anticyclonic circulation features, respectively. GoM-HYCOM = Gulf of Mexico Hybrid Coordinate Ocean Model; *MLD* = Mixed Layer Depth.

4.3. Origin of the Low-Salinity Waters Exported to the Gulf Interior

We examine the relative contribution of sources in the observed and simulated low-salinity offshore branches. The evolution of the surface salinity, averaged over three areas (Figure 1a), west and east of the LC and the Straits of Florida, is presented in Figure 16. The results from the *Realistic* reference simulation are compared with the respective salinity fields from the idealized *NoMR* (without MR input) and *NoMR/NoPrecip* (without MR and precipitation inputs) for the entire 2015. The observed mean SSS, derived from the MODIS satellite data, is also shown. All experiments revealed salinity levels higher than 36 from January to June and in December, due to the absence of southward export of low-salinity waters. The formation of the eastern branch in July and its evolution through August significantly reduced the mean salinity below 34.5. This reduction was still evident until October, as derived from both *Realistic* and observed MODIS data (Figure 16b). On the other side of the LC (western pathway), a rapid drop in salinity became significant in August and was evident over the study area until late September (Figure 16a); this reduction was smaller (down to ~35) in comparison to the eastern branch.

The removal of the MR input from the numerical simulations is designed to describe the MR contribution, in the context of freshwater inputs from other rivers and precipitation, to the formation and evolution of all branches. The MR impact was similar in both eastern and western branches, resulting comparable differences from the *Realistic* levels. The MR effect was somewhat larger in the eastern branch, showing slightly larger SSS differences ($\Delta SSS_{\text{Realistic} - \text{NoMR}} \approx 1$ in mid-August; Figure 16b) than in the western branch ($\Delta SSS_{\text{Realistic} - \text{NoMR}} \approx 0.6$ in early August; Figure 16a). The coefficients of determination between *NoMR* and *Realistic* experiments are high in both cases with lower value ($R^2 = 0.86$; Figure 16e) for the eastern branch, indicating a stronger impact of the MR. The deviation of the respective linear fit from the $x = y$

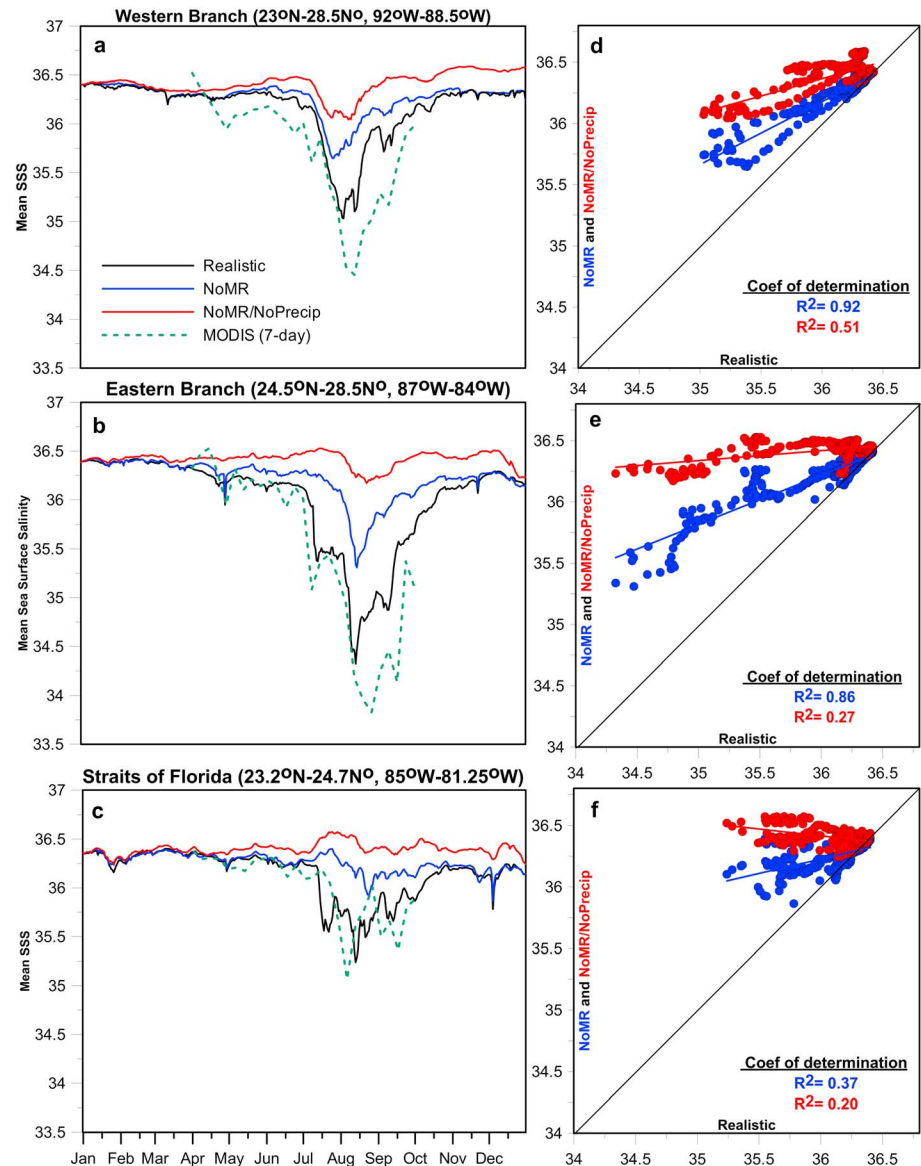


Figure 16. Daily evolution of SSS derived from the Gulf of Mexico Hybrid Coordinate Ocean Model 1/50 simulations: *Realistic* (black line), *NoMR* (blue line), and *NoMR/NoPrecip* (red line), averaged over (a) the western branch, (b) the eastern branch, and (c) the Straits of Florida (areas marked in Figure 1a) for the entire year 2015; the 7-day composite satellite SSS evolution derived from MODIS is also presented (green dashed line). Scatter diagrams of *NoMR* (blue) and *NoMR/NoPrecip* (red) experiments against the *Realistic* simulation for (d) the western branch, (e) the eastern branch, and (f) the Straits of Florida. The respective coefficients of determination, the $x = y$ identity lines and the linear fits are also shown. SSS = Sea Surface Salinity; MODIS = Moderate Resolution Imaging Spectroradiometer.

equality line was smaller in the western branch ($R^2 = 0.92$; Figure 16d). This result shows that the MR effect during summer 2015 was larger along the eastern branch, compared to the western branch, where contribution from other rivers appeared elevated.

The additional removal of freshwater input by setting precipitation to be zero (*NoMR/NoPrecip* experiment) introduced a large increase of the mean salinity in both branches. The salinity reduction in August was larger in the western (~ 0.5) than in the eastern (~ 0.3) branch, and thus, the coefficient of determination again was smaller in the eastern branch ($R^2 = 0.27$). The higher R^2 of the western branch (Figure 16d) confirms smaller contribution of both MR and precipitation to its formation, as compared to their influence on the eastern branch (larger deviation of *NoMR/NoPrecip* from *Realistic* experiment; Figure 16e). The impact of

the other rivers in the northern Gulf was higher in the western branch, possibly due to the strong discharge from the Atchafalaya River (Table 1).

The above methods were also applied to the Straits of Florida. Satellite and simulated SSS, averaged over the Straits, revealed significant drops in July and August, and the signal of brackish waters was evident until October (Figure 16c). The MR impact was stronger in late July; the *NoMR* mean salinity was significantly higher (~ 36.3) than the respective values derived from the *Realistic* simulation ($\Delta SSS_{\text{Realistic} - \text{NoMR}} \approx 0.7$). As presented in section 4.1, this period was characterized by very low precipitation rates over the Straits but with the largest MR discharge rates of the entire year that significantly reduced salinity in the Straits of Florida approximately 2 weeks later (Figure 12b). Precipitation rates over the Straits increased in the second half of August (Figure 12b), increasing the rain influence on the reduction of salinity over the area; the *NoMR* simulation revealed apparent but smaller differences against the *Realistic* simulation during the same period ($\Delta SSS_{\text{Realistic} - \text{NoMR}} \approx 0.25$). The differences between the *NoMR/Precip* and *NoMR* experiments were relatively high ($\Delta SSS_{\text{NoMR/Precip} - \text{NoMR}} \approx 0.5$), confirming the importance of the rainfall input in late August. At the same period, the MR discharge rates decreased, contributing to the weaker impact of MR input on the low-salinity values inside the Straits. Generally, the differences between the *NoMR* and *Realistic* simulations were quite large during the entire period of eastern branch spreading, having an influence inside the Straits. The lowest R^2 of the three regions was computed in the Straits of Florida ($R^2 = 0.37$; Figure 16f). However, periods with increased precipitation contribution were also detected from mid-August until the end of the low-salinity export period (October), as confirmed by the low coefficient of determination between the *Realistic* and the *NoMR/Precip* simulations ($R^2 = 0.20$; Figure 16f). Moreover, several salinity drops throughout the year were related with respective rainfalls (e.g., late April and early December; Figure 16c), although the MR discharge rates were significantly high but without forming eastern offshore branches.

5. Conclusions

This study focused on the formation and evolution of offshore pathways of river-induced low-salinity waters that originated in the northern GoM shelf areas (especially around the Mississippi Delta) and propagated southward toward the Gulf's interior and beyond. Although the offshore removal process of such waters and their near-surface pathways to the central GoM and the Straits of Florida have been studied in the past, this study provided a novel comprehensive analysis of their three-dimensional structure, evaluated their origin, and analyzed the role of both shelf circulation and basin-wide mesoscale features on their evolution. We described the formation of two dominant pathways of low-salinity waters that travel along the each side of the LC from the northern to the basin interior, extending to southern GoM and the Straits of Florida. Three distinct branches were detected in the summer of 2015. One branch evolved in July along the eastern LC boundary (eastern pathway), and two additional branches were observed along both sides (eastern and western pathways) of the LC in August. The conditions of summer 2015 were of particular interest to study these processes for two main reasons: First, unique conditions prevailed, with two simultaneous export pathways in August that resulted in extended episodes of offshore transport that reached the Straits of Florida under a variety of meteorological, river discharge, and ocean conditions. Second, unique tools were available for quantitative analyses: a data set of ship-borne profiles and glider measurements, plus a three-dimensional model with detailed river plume dynamics and realistic basin-wide mesoscale circulation.

The first condition for offshore pathways is the availability of plume waters near the shelf-break. This is usually achieved with a reversal of the buoyancy-driven downstream (westward) flow, under the influence of opposing westerly winds over the LATEX shelf. Although this process contributes to increasing the quantities of brackish waters over the eastern LATEX, it is not sufficient for offshore removal. A necessary condition for cross-marginal transport beyond the shelf-break and the initial formation of the western pathway is related to regional mesoscale processes. In particular, the combination of cyclonic and anticyclonic flows near the accumulated brackish waters is the main mechanism for creating offshore jets that initiate the southward branches. During our study period (August 2015), this condition materialized both west and east of the LC system (LC and associated eddy fields). The LC was extended far northward (28°N) near the Mississippi Delta, while the LCE extended west along the LATEX shelf-slope, separated from the LC by a strong cyclonic LCFE. The western pathway was triggered by the eastward advection of brackish waters

due to the LCE influence in the vicinity of the shelf-slope and by the two counterrotating eddies (LCE and LCFE). The eastern pathway was triggered by the LC and another LCFE. These findings extend previous studies that concentrated on the eastern pathway (Le Hénaff & Kourafalou, 2016; Ortner et al., 1995; Schiller et al., 2011; Walker et al., 2005).

The vertical structure of the offshore branches was strongly influenced by the interaction of the cyclonic LCFEs with the LC. This caused LC curvature where the low-salinity waters were confined, with a subsequent deepening of the upper layer of brackish waters. This effect was also apparent in the area between the LCE and LCFEs along the western pathway and in the Straits of Florida, under the interaction between the FC and a cyclonic eddy that evolved at the slope of the Southwestern Florida shelf. The study findings suggest that the thickness, direction, and propagation speed of the riverine low-salinity branches are highly variable and are influenced by LCFEs interacting with the LC front. This interaction weakens stratification between upper layer low-salinity and underlying waters through a convergence between these counterrotating circulation features that spreads the brackish waters toward deeper layers, increasing their vertical penetration.

The MR waters were dominant in both western and eastern pathways compared to other freshwater sources (other rivers and precipitation). The MR contribution increased the brackish signal along the eastern pathway by approximately 50%. The signal of other northern Gulf rivers was mainly detected along the western pathway. The impact of precipitation was more significant along the eastern pathway, but the overall contribution of precipitation was found minimal, in comparison to the export of brackish waters from rivers located in the northern Gulf.

The evolution of the offshore branches of waters with distinct riverine properties from the northern to the southern GoM and the Straits of Florida provides insights on the connectivity of remote GoM coastal areas through the deep basin interior. Although this is a physical study, implications on biogeochemistry can be deduced. For instance, waters of river origin may also carry nutrients, sediments, and pollutants. In addition, these pathways may provide corridors for hydrocarbons from a potential oil spill in the regions of major oil exploration in the northern GoM, allowing harmful chemicals to reach fragile coral reef ecosystems in South Florida and beyond.

References

- Androulidakis, Y., Kourafalou, V., zkgmen, T., GarciaPineda, O., Lund, B., Le Hnaff, M., et al. (2018). Influence of river-induced fronts on hydrocarbon transport: A multiplatform observational study. *Journal of Geophysical Research: Oceans*, *123*, 3259–3285. <https://doi.org/10.1029/2017JC013514>
- Androulidakis, Y. S., & Kourafalou, V. H. (2013). On the processes that influence the transport and fate of Mississippi waters under flooding outflow conditions. *Ocean Dynamics*, *63*(2-3), 143–164. <https://doi.org/10.1007/s10236-012-0587-8>
- Androulidakis, Y. S., Kourafalou, V. H., & Schiller, R. V. (2015). Process studies on the evolution of the Mississippi River plume: Impact of topography, wind and discharge conditions. *Continental Shelf Research*, *107*, 33–49. <https://doi.org/10.1016/j.csr.2015.07.014>
- Atkinson, L. P. and Tester, P. A., 1993. Low-salinity water in the Gulf Stream off North Carolina. *Coastal Oceanographic Effects of Summer*, pp.71-75.
- Atkinson, L. P., & Wallace, D. (1975, December). The source of unusually low surface salinities in the Gulf Stream off Georgia. *Deep Sea Research and Oceanographic Abstracts*, *22*(12), 913–916. [https://doi.org/10.1016/0011-7471\(75\)90093-5](https://doi.org/10.1016/0011-7471(75)90093-5)
- Bleck, R. (2002). An oceanic general circulation model framed in hybrid isopycnic-Cartesian coordinates. *Ocean modelling*, *4*(1), 55–88. [https://doi.org/10.1016/S1463-5003\(01\)00012-9](https://doi.org/10.1016/S1463-5003(01)00012-9)
- Cancet, M., Birol, F., Roblou, L., Langlais, C., Guihou, K., Bouffard, J., et al. (2009). CTOH regional altimetry products: Examples of applications. *Proceedings of Ocean Observations*, *9*, 306.
- Chen, S., & Hu, C. (2017). Estimating sea surface salinity in the northern Gulf of Mexico from satellite ocean color measurements. *Remote Sensing of Environment*, *201*, 115–132. <https://doi.org/10.1016/j.rse.2017.09.004>
- Cochrane, J. D., & Kelly, F. J. (1986). Low-frequency circulation on the Texas-Louisiana continental shelf. *Journal of Geophysical Research*, *91*(C9), 10,645–10,659. <https://doi.org/10.1029/JC091iC09p10645>
- Csanady, G. T. (1984). The free surface turbulent shear layer. *Journal of physical oceanography*, *14*(2), 402–411. [https://doi.org/10.1175/1520-0485\(1984\)014<0402:TFSTSL>2.0.CO;2](https://doi.org/10.1175/1520-0485(1984)014<0402:TFSTSL>2.0.CO;2)
- Dinnel, S. P., & Wiseman, W. J. Jr. (1986). Fresh water on the Louisiana and Texas shelf. *Continental Shelf Research*, *6*(6), 765–784. [https://doi.org/10.1016/0278-4343\(86\)90036-1](https://doi.org/10.1016/0278-4343(86)90036-1)
- Felton, C. S., Subrahmanyam, B., Murty, V. S. N., & Shriver, J. F. (2014). Estimation of the barrier layer thickness in the Indian Ocean using Aquarius Salinity. *Journal of Geophysical Research: Oceans*, *119*, 4200–4213. <https://doi.org/10.1002/2013JC009759>
- Fournier, S., Reager, J. T., Lee, T., Vazquez-Cuervo, J., David, C. H., & Gierach, M. M. (2016). SMAP observes flooding from land to sea: The Texas event of 2015. *Geophysical Research Letters*, *43*, 10–338. <https://doi.org/10.1002/2016GL070821>
- Garvine, R. W. (1987). Estuary plumes and fronts in shelf waters: A layer model. *Journal of Physical Oceanography*, *17*(11), 1877–1896. [https://doi.org/10.1175/1520-0485\(1987\)017<1877:EPAFIS>2.0.CO;2](https://doi.org/10.1175/1520-0485(1987)017<1877:EPAFIS>2.0.CO;2)
- Gierach, M. M., Vazquez-Cuervo, J., Lee, T., & Tsontos, V. M. (2013). Aquarius and SMOS detect effects of an extreme Mississippi River flooding event in the Gulf of Mexico. *Geophysical Research Letters*, *40*, 5188–5193. <https://doi.org/10.1002/grl.50995>

Acknowledgments

This research was made possible in part by two grants from The Gulf of Mexico Research Initiative (Awards GOMA23160700 and DEEPEND: GOMRI2014-IV-914) and in part by the National Oceanic and Atmospheric Administration (NOAA) Center for Sponsored Coastal Ocean Research under Award NA11NOS4780045 to the University of Miami (Project Title: “Connectivity of the Pulley Ridge – South Florida Coral Reef Ecosystem”) and by the NOAA’s RESTORE Act Science Program under Award NA15NOS4510226 to the University of Miami. Additional support to the authors was made possible through NOAA Award NA15OAR4320064 to UM/RSMAS and through NASA Award NNX14AL98G and NOAA Award NA17NOS4510099 to USF. Matthieu Le Hénaff received partial support for this work from the base funds of the NOAA Atlantic Oceanographic and Meteorological Laboratory. Data are publicly available through the Gulf of Mexico Research Initiative Information & Data Cooperative (GRIIDC); <https://data.gulfresearchinitiative.org>; Slocum glider: doi: 10.7266/N7VM49MP; DEEPEND observations: doi: 10.7266/N7PV6HS1; GoM-HYCOM fields: doi: 10.7266/n7-3s8f-m404 and doi: 10.7266/n7-4zwa-jj02). Altimetry data used in this study were developed, validated, and distributed by the CTOH/LEGOS, France (doi: 10.6096/CTOH_X-TRACK_2017_02). This study has been conducted using E.U. Copernicus Marine Service Information. The high-resolution ocean chl-*a* images and SSS fields were developed in the Optical Oceanography Laboratory (University of South Florida), based on the MODIS data, which are openly accessible from NASA (<https://oceancolor.gsfc.nasa.gov/>).

- Gilbert, P. S., Lee, T. N., & Podesta, G. P. (1996). Transport of anomalous low-salinity waters from the Mississippi River flood of 1993 to the Straits of Florida. *Continental Shelf Research*, *16*(8), 1065–1085. [https://doi.org/10.1016/0278-4343\(95\)00056-9](https://doi.org/10.1016/0278-4343(95)00056-9)
- Halliwell, G. R. Jr., Kourafalou, V., Le Hénaff, M., Shay, L. K., & Atlas, R. (2015). OSSE impact analysis of airborne ocean surveys for improving upper-ocean dynamical and thermodynamical forecasts in the Gulf of Mexico. *Progress in Oceanography*, *130*, 32–46. <https://doi.org/10.1016/j.pocean.2014.09.004>
- Halliwell, G. R. Jr., Srinivasan, A., Kourafalou, V., Yang, H., Willey, D., Le Hénaff, M., & Atlas, R. (2014). Rigorous evaluation of a fraternal twin ocean OSSE system for the open Gulf of Mexico. *Journal of Atmospheric and Oceanic Technology*, *31*(1), 105–130. <https://doi.org/10.1175/JTECH-D-13-00011.1>
- Hickey, B. M., Pietrafesa, L. J., Jay, D. A., & Boicourt, W. C. (1998). The Columbia River plume study: Subtidal variability in the velocity and salinity fields. *Journal of Geophysical Research*, *103*(C5), 10,339–10,368. <https://doi.org/10.1029/97JC03290>
- Hu, C., Muller-Karger, F. E., Biggs, D. C., Carder, K. L., Nababan, B., Nadeau, D., & Vanderbloemen, J. (2003). Comparison of ship and satellite bio-optical measurements on the continental margin of the NE Gulf of Mexico. *International Journal of Remote Sensing*, *24*(13), 2597–2612. <https://doi.org/10.1080/0143116031000067007>
- Hu, C., Nelson, J. R., Johns, E., Chen, Z., Weisberg, R. H., & Müller-Karger, F. E. (2005). Mississippi River water in the Florida Straits and in the Gulf Stream off Georgia in summer 2004. *Geophysical Research Letters*, *32*, L14606. <https://doi.org/10.1029/2005GL022942>
- Kourafalou, V. H. (2001). River plume development in semi-enclosed Mediterranean regions: North Adriatic Sea and northwestern Aegean Sea. *Journal of Marine Systems*, *30*(3–4), 181–205. [https://doi.org/10.1016/S0924-7963\(01\)00058-6](https://doi.org/10.1016/S0924-7963(01)00058-6)
- Kourafalou, V. H., & Androulidakis, Y. S. (2013). Influence of Mississippi River induced circulation on the Deepwater Horizon oil spill transport. *Journal of Geophysical Research: Oceans*, *118*, 3823–3842. <https://doi.org/10.1002/jgrc.20272>
- Kourafalou, V. H., & Kang, H. (2012). Florida Current meandering and evolution of cyclonic eddies along the Florida Keys Reef Tract: Are they interconnected? *Journal of Geophysical Research*, *117*, C05028. <https://doi.org/10.1029/2011JC007383>
- Kourafalou, V. H., Oey, L. Y., Wang, J. D., & Lee, T. N. (1996). The fate of river discharge on the continental shelf: 1. Modeling the river plume and the inner shelf coastal current. *Journal of Geophysical Research*, *101*(C2), 3415–3434. <https://doi.org/10.1029/95JC03024>
- Le Hénaff, M., & Kourafalou, V. H. (2016). Mississippi waters reaching South Florida reefs under no flood conditions: Synthesis of observing and modeling system findings. *Ocean Dynamics*, *66*(3), 435–459. <https://doi.org/10.1007/s10236-016-0932-4>
- Leben, R. R. (2005). Altimeter-derived loop current metrics. In *Circulation in the Gulf of Mexico: Observations and models*, (pp. 181–201). Washington, DC: American Geophysical Union.
- Leung, P., Perry, R., Sharma, N., Zwissler, C., McCall, W., Bouchard, R.H. and Martin, K.M., 2016, February. 2014 & 2015 Loop current observations from a Gulf of Mexico public-private ocean observing collaboration. In *American Geophysical Union, Ocean Sciences Meeting 2016*, abstract# OD14A-2405.
- Lewis, K., & Allen, J. I. (2009). Validation of a hydrodynamic-ecosystem model simulation with time-series data collected in the western English Channel. *Journal of Marine Systems*, *77*(3), 296–311. <https://doi.org/10.1016/j.jmarsys.2007.12.013>
- Martínez-López, B., & Zavala-Hidalgo, J. (2009). Seasonal and interannual variability of cross-shelf transports of chlorophyll in the Gulf of Mexico. *Journal of Marine Systems*, *77*(1–2), 1–20. <https://doi.org/10.1016/j.jmarsys.2008.10.002>
- Meade, R. H., & Moody, J. A. (2010). Causes for the decline of suspended-sediment discharge in the Mississippi River system, 1940–2007. *Hydrological Processes: An International Journal*, *24*(1), 35–49.
- Merrell, W. J., & Morrison, J. M. (1981). On the circulation of the western Gulf of Mexico with observations from April 1978. *Journal of Geophysical Research*, *86*(C5), 4181–4185. <https://doi.org/10.1029/JC086iC05p04181>
- Morey, S. L., Martin, P. J., O'Brien, J. J., Wallcraft, A. A., & Zavala-Hidalgo, J. (2003). Export pathways for river discharged fresh water in the northern Gulf of Mexico. *Journal of Geophysical Research*, *108*(C10), 3303. <https://doi.org/10.1029/2002JC001674>
- Nababan, B., Muller-Karger, F. E., Hu, C., & Biggs, D. C. (2011). Chlorophyll variability in the northeastern Gulf of Mexico. *International Journal of Remote Sensing*, *32*(23), 8373–8391. <https://doi.org/10.1080/01431161.2010.542192>
- Nowlin, W. D., Jochens, A. E., DiMarco, S. F., Reid, R. O., & Howard, M. K. (2005). *Low-frequency circulation over the Texas-Louisiana continental shelf*, *Geophysical Monograph*, (Vol. 161, p. 219). Washington, DC: American Geophysical Union.
- Nürnberg, D., Ziegler, M., Karas, C., Tiedemann, R., & Schmidt, M. W. (2008). Interacting loop current variability and Mississippi River discharge over the past 400 kyr. *Earth and Planetary Science Letters*, *272*(1–2), 278–289. <https://doi.org/10.1016/j.epsl.2008.04.051>
- Oey, L. Y. (1995). Eddy- and wind-forced shelf circulation. *Journal of Geophysical Research*, *100*(C5), 8621–8637. <https://doi.org/10.1029/95JC00785>
- Ortner, P. B., Lee, T. N., Milne, P. J., Zika, R. G., Clarke, M. E., Podesta, G. P., et al. (1995). Mississippi River flood waters that reached the Gulf Stream. *Journal of Geophysical Research*, *100*(C7), 13,595–13,601. <https://doi.org/10.1029/95JC01039>
- Roblou, L., Lamouroux, J., Bouffard, J., Lyard, F., Le Hénaff, M., Lombard, A., et al. (2011). Post-processing altimeter data toward coastal applications and integration into models. In S. Vignudelli, A. G. Kostianoy, P. Cipollini, & J. Benveniste (Eds.), *Coastal Altimetry* (pp. 217–246). Berlin, Heidelberg: Springer.
- Schiller, R. V., & Kourafalou, V. H. (2010). Modeling river plume dynamics with the HYbrid Coordinate Ocean Model. *Ocean Modelling*, *33*(1–2), 101–117. <https://doi.org/10.1016/j.ocemod.2009.12.005>
- Schiller, R. V., & Kourafalou, V. H. (2014). Loop current impact on the transport of Mississippi River waters. *Journal of Coastal Research*, *30*(6), 1287–1306.
- Schiller, R. V., Kourafalou, V. H., Hogan, P., & Walker, N. D. (2011). The dynamics of the Mississippi River plume: Impact of topography, wind and offshore forcing on the fate of plume waters. *Journal of Geophysical Research*, *116*, C06029. <https://doi.org/10.1029/2010JC006883>
- Schroeder, W. W., Dinnel, S. P., Wiseman, W. J. Jr., & Merrell, W. J. Jr. (1987). Circulation patterns inferred from the movement of detached buoys in the eastern Gulf of Mexico. *Continental Shelf Research*, *7*(8), 883–894. [https://doi.org/10.1016/0278-4343\(87\)90004-5](https://doi.org/10.1016/0278-4343(87)90004-5)
- Walker, N. D., Fargion, G., Rouse, L. J. Jr., & Biggs, D. (1994). Circulation of Mississippi River water discharged into the northern Gulf of Mexico by the great flood of summer 1993. *Eos, Transactions of the American Geophysical Union*, *75*(36), 409. <https://doi.org/10.1029/94EO01045>
- Walker, N. D., Leben, R. R., & Balasubramanian, S. (2005). Hurricane-forced upwelling and chlorophyll *a* enhancement within cold-core cyclones in the Gulf of Mexico. *Geophysical Research Letters*, *32*, L18610. <https://doi.org/10.1029/2005GL023716>
- Yuan, J., Miller, R. L., Powell, R. T., & Dagg, M. J. (2004). Storm-induced injection of the Mississippi River plume into the open Gulf of Mexico. *Geophysical Research Letters*, *31*, L09312. <https://doi.org/10.1029/2003GL019335>
- Zhang, X., Hetland, R. D., Marta-Almeida, M., & DiMarco, S. F. (2012). A numerical investigation of the Mississippi and Atchafalaya freshwater transport, filling and flushing times on the Texas-Louisiana Shelf. *Journal of Geophysical Research*, *117*, C11009. <https://doi.org/10.1029/2012JC008108>